Journal of Energy Storage 59 (2023) 106531

Contents lists available at ScienceDirect

Journal of Energy Storage

journal homepage: www.elsevier.com/locate/est

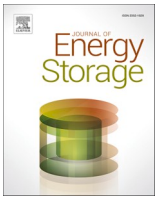

Research Papers

# The effect of melting point and combination of phase change materials on the thermal control performance of small satellites in the thermal environment of low earth orbit: Numerical study

Abdelrahman M. Elshaer [a,b], A.M.A. Soliman [a,c], M. Kassab [b], A.A. Hawwash [a,*]

[a] Mechanical engineering department, Benha faculty of engineering, Benha University, Benha, Egypt
[b] Egyptian space agency, Cairo, Egypt
[c] Faculty of Engineering and Technology, Badr University in Cairo, Cairo, Egypt

ARTICLE INFO

*Keywords:*
Thermal storage panel (TSP)
Low earth orbit
PCM combinations
Satellite thermal control
Small satellites
PCM melting temperature

ABSTRACT

Thermal management of small satellites in the thermal environment of low earth orbit is a crucial task. Any satellite in low earth orbit is subjected to two distinct thermal conditions for the duration of its orbit: extreme hotness and extreme coldness. Phase change materials (PCM) are promising candidates for the thermal control of small satellites in low earth orbit thermal conditions. The present work provides a numerical analysis of a thermal storage panel (TSP) using PCM. The TSP is used to improve small satellites' thermal control performance in the thermal environment of a low earth orbit. An aluminium TSP is designed based on a typical space-approved small satellite battery. It is integrated with five internal fins as a thermal conductivity enhancer. The fins divide the heat sink into six cuboid cavities and are filled with PCM. Three-PCM materials with melting points of 15 °C, 21 °C, and 26 °C are used. The proposed low earth orbit is at an altitude of 500 km and a beta angle of $0^0$; this resulted in an eclipse fraction of 0.37. The TSP is investigated under three levels of heating loads: 10W and 13 W. The TSP is investigated using both single and combinations of PCM. Four combination cases are investigated: (RT 15 & RT 21), (RT 21 & RT 26), (RT 15 & RT 26), and (RT 15 & RT 21 & RT 26). The results report a significant enhancement in the thermal control performance of the PCM-based TSP. At 10W and steady-state conditions, RT 15 records maximum extrema of 21.4 °C with a decreasing percentage of 34.6 % compared to the case without PCM. In addition, RT 15 records minimum extrema of 7.8 °C with an increase of 162.4 %. TSP with PCM combinations achieve a nearly constant PTD under varying heating loads and hence a constant temperature response amplitude. In addition, the PCM combinations achieve a nearly fixed specific heat with the change in heating load.

## 1. Introduction

Satellites are orbiting the earth in low earth orbit (LEO) experience an extreme thermal environment. The satellite once existed in the zone between the sun and the earth, called the sunlit zone, and other times existed in the zone of earth's shadow, which is called the eclipse zone. On the one hand, during the sunlit zone, the satellite receives a high amount of thermal energy from the sun, which results in an overheating of the satellite subsystems. On the other hand, when the satellite exists in the eclipse zone, the satellite subsystems experience a severe loss in their temperatures due to the absence of solar heat energy in the eclipse zone [1].

Satellite subsystems have a safe operating temperature range within which they operate efficiently. Satellite thermal control subsystems (TCSs) guarantee that all satellite subsystems are working in their optimal thermal conditions in both hot and cold cases. Furthermore, TCS protects other satellite subsystems from failure due to unacceptable thermal conditions [2]. TCSs are generally divided into two classifications: passive TCSs and active TCSs. Passive TCSs include multi-layer insulation (MLI), surface coatings, radiators, heat pipes, and thermal energy storage materials (TES) [3–5]. Active TCSs require a power source, such as heaters, louvers, radiators, pumped-fluid loops, heat pumps, refrigerators, and thermo-electric coolers [6].

In general, the sources of heat the spacecraft experience in LEO are 1. the direct-solar radiation incident on the spacecraft. 2. the diffusive earth radiation, which is called Albedo. 3. Infrared rays (IR) radiated

* Corresponding author.
*E-mail address:* ahmed.hawash@ejust.edu.eg (A.A. Hawwash).

https://doi.org/10.1016/j.est.2022.106531
Received 30 August 2022; Received in revised form 13 December 2022; Accepted 22 December 2022
Available online 29 December 2022
2352-152X/

from the earth. 4. The molecular heating effect is caused by friction between spacecraft and gas molecules in the space environment. 5. the energy dissipated from the avionics systems [7]. Fig. 1 presents the heat sources of LEO.

Recently, the electronic devices, and their related components used in the spacecraft industry, especially for satellite subsystems, are getting compact and have a significant power density. This results in an urgent need to develop innovative solutions for efficient thermal management of satellite subsystems. Also, the power consumed by these electronic devices is increasing. The satellite subsystems usually have a cyclic operation mode in which they are "ON" for some time, generating heat energy, and "OFF" for the rest of the cycle with limited heat generated.

## Nomenclature

*English symbols*

| | |
|---|---|
| $A_s$ | surface area ($m^2$) |
| $C_P$ | specific heat (J/kg. K) |
| H | enthalpy (J/kg) |
| $H_s$ | sensible enthalpy (J/kg) |
| $H_l$ | latent enthalpy (J/kg) |
| K | thermal conductivity (W/m. K) |
| LH | latent heat (J/kg) |
| $M_{TSP}$ | mass of thermal storage panel (kg) |
| Q | heat load (W) |
| t | time (S) |
| T | temperature (K) |

*Greek symbols*

| | |
|---|---|
| ρ | density ($Kg/m^3$) |
| α | absorptivity |
| ε | emissivity |
| σ | Stefan- Boltzmann constant ($W/m^2$. K) |
| μ | dynamic viscosity (Kg/m. s) |

*Abbreviations*

| | |
|---|---|
| ADCS | Attitude determination and control subsystem |
| CFRP | Carbon fiber reinforced polymer |
| CNT | Carbon nanotube |
| GOP | Graphene oxide particles |
| LHS | Latent heat storage |
| LEO | Low earth orbit |
| MLI | Multi-layer insulation |
| PCM | Phase change materials |
| PRESTO | Pressure staggering options |
| PTD | Peak temperatures difference |
| SHS | Sensible heat storage |
| SS-PCM | Solid-solid phase change materials |
| TCE | Thermal conductivity enhancer |
| TCS | Thermal control subsystem |
| TES | Thermal energy storage materials |
| TSP | Thermal storage panel |
| TCM | Thermal control module |
| TVC | Thermal vacuum chamber |

*Subscript*

| | |
|---|---|
| app | apparent |
| i | initial |
| rad | radiation |
| S | solar |
| L | heat load |
| max | maximum |

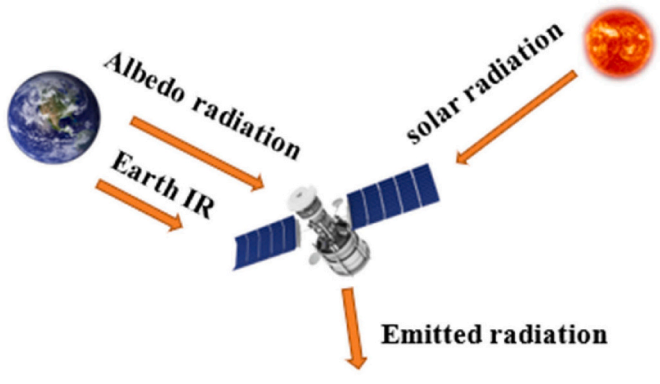


**Fig. 1.** The sources of heat the spacecraft experiences in LEO environment.

Thermally critical satellite subsystems require more thermal constraints and have a limited span of the operating temperature range. These critical subsystems include remote sensing, optical, battery, and microwave satellite payloads. In these subsystems, a high quantity of heat is produced over a short time during the "ON" mode before they enter again to "OFF" mode, and heat generation stops [8,9]. Among the satellite components, the battery involves the most severe temperature limitations of satellite components with an allowable temperature range in general from $-10\,^{\circ}C$ to $50\,^{\circ}C$ [10]. There is a distinction between the thermal conditions of small satellites, of the category micro/nanosatellites, and large satellites in space. Small satellites have (i) small heat capacity, (ii) limited power resources, (iii) relatively small radiator areas, (iv) highly compact electronics, and (v) mass constraints. That's why micro/nanosatellites are less thermally controllable than large satellites. Recently, Nasa reported a problem in one of its nanosatellites of NASA's Edison Demonstration of Small sat Networks (EDSN). The satellite has been restricted in its operating time due to the heat dissipation generated by mission devices [11].

Improving thermal controllability for small satellites requires a novel thermal control subsystem. This novel TCS needs to account for mass and size limitations in micro/nanosatellites and consumes no electrical power. TES are promising candidates for solving micro/nano satellites' thermal controllability issues. Using TES in satellite thermal control is a passive technique for small satellite thermal control with no power requirements. Many researchers focus on the implementation and feasibility of using TES in the thermal control of small satellites. Two types of TES are used in satellite TCSs: latent heat storage (LHS) and sensible heat storage (SHS) materials. Both techniques of TES were used in the thermal control of satellite subsystems. LHS materials store heat energy as they experience a phase change process or change in their crystalline structure (solid-solid phase change materials (SS-PCM)).

A numerical study by Madruga et al. [12] investigated the effect of nano-metallic particles on thermal energy storage and heat transfer in a PCM forced by thermocapillary. The findings concluded that metallic nanoparticles with higher diameters support higher convective flows and better heat transfer. Madruga and Mendoza [13] delivered a numerical study simulating the melting process of the PCM in squared geometries under the natural convection and thermocapillary effects. The PCM used was n-octadecane. The results revealed that thermocapillary effects at a small Bond number significantly enhance the heat transfer rate. Swanson et al. [14] surveyed to summarize the current efforts at the National Aeronautics and Space Administration to develop new technologies of thermal control systems for future robotic missions. Giangi et al. [15] reported a numerical study investigating the significance of Marangoni effects in microgravity conditions. The findings revealed that the presence of the argon and Marangoni convection play a vital role in affecting the solidification process.

Shukla and Ababneh et al. [16,17] examined the thermal performance of the heat pipes using LHS materials of (water, ammonia, and

ethylene glycol). LHS materials were fitted in the heat pipes as the working fluids and were coupled with radiators for thermal control of satellite subsystems. Thermal control of small satellites using (PCM) as LHS materials is a promising solution for small satellites' thermal controllability issues. PCM can raise the apparent heat capacity for the small satellite subsystems. Therefore, PCM can reduce the temperature fluctuation that satellite subsystems experience in space. Thermal control of small satellites using PCM is a passive thermal control technique that requires no electrical power and accounts for the mass constraints of small satellites. Madruga et al. [18] conducted a numerical study about the melting dynamics of a PCM by the action of the thermocapillary effect. The results reported enhancement in the heat transfer of PCM by thermocapillary effect.

The effective way to use PCM in the thermal control of satellite avionics is by using PCM encapsulation. PCM encapsulation refers to encapsulating the PCM inside a container with an appropriate design to accommodate the PCM. The main objective of PCM encapsulation is to keep the PCM's solid and/or liquid phase and isolate it from its surroundings. Hence, PCM encapsulation ensures a fixed PCM composition that could be changed due to exposure to the surroundings [19,20]. Research using PCM encapsulated in thermal control modules (TCM) has flourished recently. Hansen et al. and Humphries [21,22] studied the process of PCM phase change under normal and zero-gravity conditions in 1974. Abhat and Groll [23], studied using a honeycomb structure as a filler material in the PCM-based thermal control module. The authors reported the effectiveness of the honeycomb structure in limiting the hardware temperature within narrow bands as required for the satellite operating conditions. In addition, the authors concluded that the natural convection effects within the PCM are negligible for space applications. Three PCM-based-thermal capacitors were manufactured and tested for ExoMars 2016 European space agency mission [24]. The thermal capacitors contain phase change waxes to absorb the heat energy during the phase transition process.

Baby and Balaji [25] conducted an experimental investigation about the effect of using PCM-based finned heat sinks for the thermal management of electronic devices. The PCM used was n-eicosane encapsulated in an aluminium-finned heat sink. The aluminium fins of the heat sink are used as a thermal conductivity enhancer to compensate for the low values of PCM thermal conductivity. The study reported a significant improvement in the heat sink's thermal performance by using aluminium fins as a thermal conductivity enhancer. Baby and Balaji [26] experimentally studied the effect of fins configuration for a PCM-based heat sink and the PCM type on the thermal performance of electronics. Both n-eicosane and paraffin wax were used individually as the PCM. The results revealed that paraffin wax was better than n-eicosane for maintaining the hardware temperature within the desired range. Madruga et al. [27] presented a new concept of harvesting electrical energy from ambient thermal fluctuations using the Marangoni effect, thermoelectric generators, and PCM. The results show that this type of micro-harvesters obtained high specific power.

Wu et al. [28] conducted a numerical study about the effectiveness of a shape-stabilized PCM module in protecting the satellite against a short-term high-level heat flux. In this study, one side of the satellite model was subjected to a high heat flux of 3 $W/cm^2$ for 100 s. The results show that the shape-stabilized PCM module was highly influential in absorbing short-term high heat flux and protecting the satellite from extreme temperature values. The development of a novel thermal control module named a heat storage panel was performed by Yamada and Nagano [10]. In this study, Eicosane was inserted into the heat storage panel as a PCM, while carbon fiber-reinforced polymer was utilized as a thermal conductivity enhancer. The novel HSP was demonstrated early in orbit. Kim et al. [29] reported A new spacecraft TCM in a numerical study. This study used heat pipes as a thermal conductivity enhancer for PCM, while alkane was used as a PCM with a melting point of 28°$C$. A numerical study on the effect of using expanded graphite to increase the thermal conductivity of shape-stabilized PCM used for electronic devices' thermal control was conducted by Cheng et al. [30]. The results depicted a significant improvement in the thermal conductivity of PCM to four times higher than that of the original one.

Mahmoud et al. [31] conducted an experimental study about the effects of PCM, power levels, and design of heat sink configuration on PCM-based TCM performance for the cooling process of electronic devices. The study revealed a significant enhancement in the thermal performance at a higher number of fins for both parallel and cross-fin geometries. An experimental and numerical investigation was carried out by Yang et al. [32] to study using low melting point PCM in a metal-based heat sink. Aluminium fins were used as thermal conductivity enhancers (TCE), and several internal fins were studied in the heat sink. An experimental study was performed by Praveen and Suresh [33] to investigate the thermal performance of a PCM microencapsulation technique using low melting alloy as a TCE. The results show a significant enhancement in the thermal performance using PCM microencapsulation with low melting alloy. The study delivered a uniform temperature distribution in the PCM with a complete melting of the PCM. A numerical investigation was performed by Desai et al. [34] to find out the most effective fin configuration of an aluminium finned PCM heat sink. Four fin parameters were tested: size, number, shape, and mass percentage of fins.

Raj et al. [35] carried out a numerical investigation about the effect of fin configuration on the performance of a satellite thermal control module using SS-PCM. This study investigated the effect of fin thickness, fin shape, TCM base thickness, and the number of fins for a steady heat flux. Ho et al. [36] experimentally examined a PCM-based heat sink's thermal performance using a tree-like structure TCE. The study reported the potential of tree-like structures to enhance thermal performance. A numerical study performed by Kansara et al. [37] studied the effect of gravity on PCM's solidification and melting processes in an optimized TCM with fins (pin type) as heat transfer enhancers. Pakrouh et al. [38] performed a numerical investigation about a geometric optimization for PCM-based heat sinks with pin fin. RT 44 HC was used as a PCM, while the Taguchi method was used for the experiment design. Results show the high dependency of the optimal thermal performance case on the number, height, and thickness of fins and the critical temperature of the TCM. An experimental study about the enhancement of PCM-based TCM thermal performance and the effects of TCM orientation was presented by Baby and Balaji [39]. N-eicosane was used as the PCM, while a copper open-cell metal foam was adopted as a TCE. The results revealed that the TCM orientation did not have an interesting effect on its thermal performance.

Gharbi et al. [40] compared experimentally different PCM-based heat sink configurations and their impact on the thermal control performance of electronic components. At the same time, Xu et al. [41] Presented a novel microchannel PCM-based heat sink for thermal control applications. Carbon nanotubes (CNTs) and Graphene Oxide particles (GOPs) were used as TCE. The results revealed a significant improvement in the heat sink's thermal performance by adding CNTs and GOPs. Saha et al. [42] studied the effect of TCE volume fraction on the thermal control performance of PCM - based heat sinks. The results reported that the TCE volume fraction of 8 % gave the best thermal performance of the heat sink when aluminium was used as the TCE material.

Ye et al. [43] presented a novel composite PCM with dual phase change temperature regions. The novel composite PCM designed with phase changeable polymer presented better thermal management in cooling the battery than the traditional composite PCM. Younis et al. [44] presented a numerical study investigating the heat energy storage performance of nano-improved PCM. The results showed a significant improvement in energy storage performance by using nanoparticles integrated with PCM. Li et al. [45] presented a novel kind of flexible PCM by a solvent-evaporation method at room temperature. The findings reported the flexible PCM produced by the solvent-evaporation method is promising for future applications. An experimental and

numerical study by Hu et al. [46] investigated a heat pipe/PCM composite for the thermal management of lithium-ion batteries. Results show that the heat pipe/PCM composite system outperforms the heat pipe-assisted battery thermal management system regardless of the battery discharge rate. Wu et al. [47] studied a flexible PCM that can minimize the thermal contact resistance for the thermal management of batteries. The results reported a significant improvement in the thermal management performance of the flexible PCM and the Rigid PCM.

## 2. Purpose of the present research

This study presents a numerical thermal analysis of a proposed thermal storage panel (TSP) for the thermal control of small satellites in low earth orbit. The TSP was an aluminium heat sink integrated with PCM. The effect of PCM melting point on the thermal control performance of TSP was investigated. Furthermore, the effects of using phase change materials combinations for thermal control of satellite avionics in the space environment were studied. The objective of the current work is to examine the effect of PCM melting point and PCM combination on the thermal performance of a PCM-based TSP. In two cases, the proposed TSP was tested for the thermal management of satellite avionics in the space environment. The TSP contained a single PCM with one melting point in the first case. But in the second case, the TSP contained a combination of PCM. The PCM combination cases had two scenarios. First, the TSP was filled with two PCM. Second, the TSP was filled with three PCM. Each PCM was separated in its cavity without mixing in PCM combination cases. The PCM combination cases have different melting points, including double and triple PCM. The heat sink model was integrated with fins for applying the PCM combination in the same heat sink, resulting in separated cavities for accommodating PCM without mixing. The fins also work as a thermal conductivity enhancer to enhance PCM thermal conductivity's moderate values.

The novelty in the present work is presented in the following points.

- The PCM-based TSP was tested and analyzed under the actual intermittent thermal environment of a proposed low earth orbit for several orbits.
- The TSP was designed based on a typical small satellite configuration.
- Three-dimensional transient numerical investigation about the effect of PCM melting point and PCM combination on a PCM-based TSP's thermal control performance under different heating loads.
- The effects of PCM combination on the stability of the thermal response with a varying heating load.

## 3. Model description and materials

This work investigates a TSP designed based on the typical configurations of a small satellite project. The outer dimensions of the TSP were selected to be compatible with the outer dimensions of the satellite. This satellite was nearly a cube of 60 kg in weight and had a side length of 0.8 m. The TSP location was selected carefully according to the satellite configuration and temperature distribution. In the present model, The TSP consisted of a heat sink with integrated fins manufactured from aluminium 6061 (T6). Aluminium was selected due to its relatively high thermal conductivity of 167.9 W/m. k, relatively low density among other metals of 2770 $kg/m^3$ and hence, lower mass which has a significant concern in spacecraft design. The heat sink was integrated with six aluminium parallel fins, resulting in six separated cuboid cavities within the body of the heat sink. Later, the heat sink cavities were filled with PCM to study the effect of PCM melting point and PCM combination on the thermal control performance of the heat sink.

The heat sink's outer dimensions were designed based on a typical small satellite configuration. The heat sink's length, width, and height are 98 mm, 71 mm, and 22 mm, respectively. Parallel fins were used as thermal conductivity enhancers (TCE) to overcome the relatively low PCM thermal conductivity. In the present study, five parallel fins were milled in the heat sink, resulting in six cavities of 13 mm in width and 61 mm in length, and 12 mm in height. A TCE volume fraction of 8 % was used in the present work, resulting in a fin thickness of 2 mm. The thicknesses of the cover plate, base plate, and side walls were all 5 mm. The detailed heat sink dimensions and configuration are shown in Figs. 2 and 3, respectively. The volume of the TSP elements and weight for all cases studied are presented in Tables 1 and 2, respectively. The average total weight of the TSP was nearly 316.2 g. While the total volume of the TSP was 98 mm, 71 mm, and 22 mm in length, width, and height, respectively.

Fig. 4 presents the small satellite dummy model with the TSP mounted on its back plate. This project is carried out between Benha university and the Egyptian space agency. The satellite Model was of the microsatellite category with a total mass of 45 Kg and volume of 40 cm * 40 cm * 30 cm in length, width, and height, respectively. The TSP was mounted on the satellite back plate. Fig. 4 (a) presents the location of the TSP on the satellite back plate. While Fig. 4 (b) presents, the subsystems mounted to the plate. These subsystems were the significant sources of hardware heat load that the TSP experiences during operation.

Table 1 presents the typical heat load experienced by the subsystems of interest. The sum of these loads was 9.2 W, rounded to 10 W. Considering the uncertainty in the heat load values and optimizing our model by maximizing the heat load; the TSP was also tested at 13 W with a 30 % increase to the calculated heat load. Tables 2 and 3 present the TSP elements' volume and weight, respectively. The total volume and average weight of the TSP were 153.07 $cm^3$ and 316.1 g, respectively.

The TSP cover plate was anodized with a black coating. The black anodization had a solar absorptivity and emissivity of 0.65 and 0.82, respectively. The cover plate acted as a thermal radiator which emitted the absorbed heat to the surrounding space. The TSP was solved under the orbital conditions as a radiator only without PCM to select the appropriate PCM melting points. The appropriate PCM melting points must be within the temperature results margins for the radiator to store the thermal energy during phase transition. The used PCM were all organic-based materials. Organic-based PCM has high thermal stability when subjected to continuous phase change cycles. The PCM used are commercial materials from (Rubitherm GmbH) [48]. The

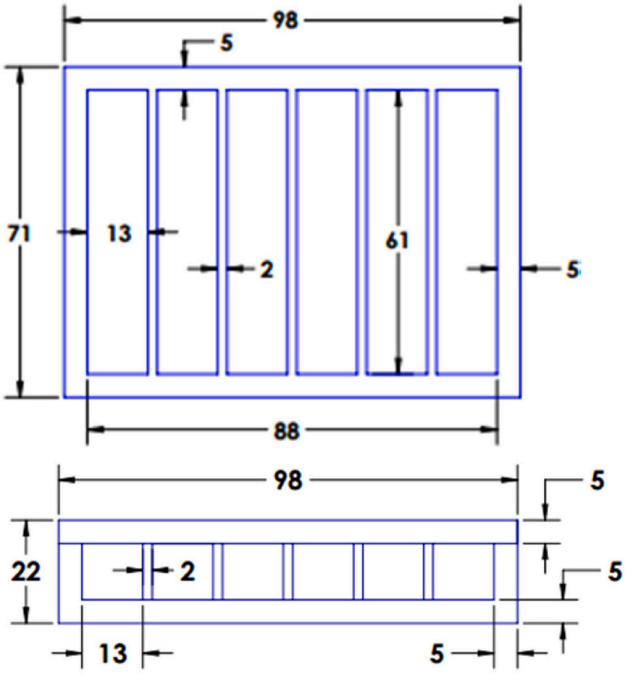


**Fig. 2.** TSP dimensions and configuration (dimensions are in mm).

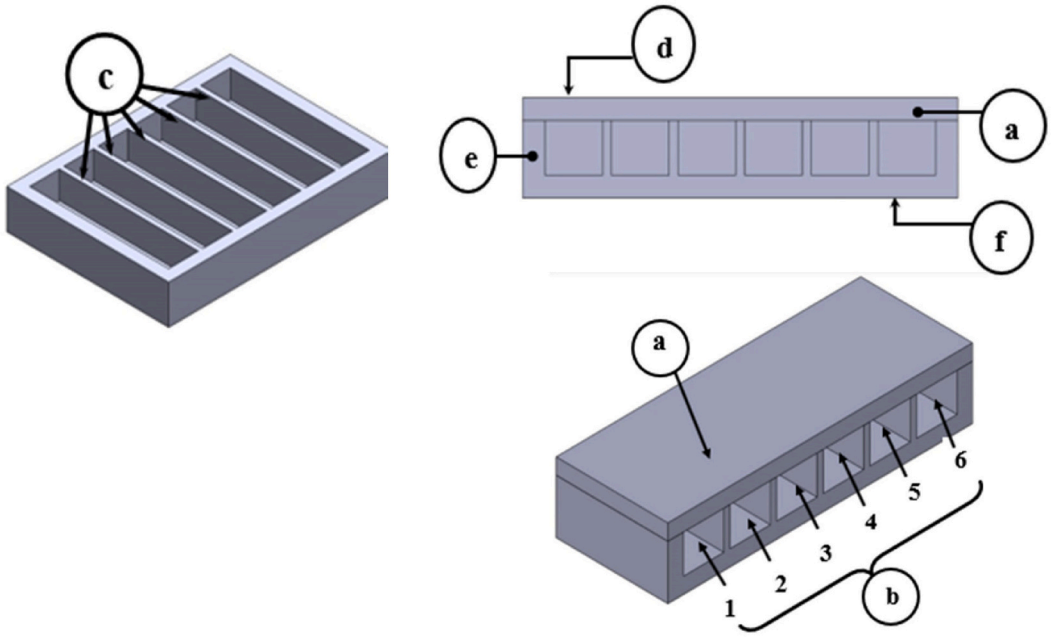


**Fig. 3.** TSP parts description and configuration (a) Cover plate, (b) PCM cavities numbered from 1 to 6, (c) Fins, (d) Top plate surface (Radiator), (e) TSP side walls, (f) Base plate (Heat source).

**Table 1**
Typical heat load of satellite subsystems mounted on the TSP plate.

| Subsystem | Quantity | Heat load (W) |
|---|---|---|
| Reaction wheel | 1 | 0.5 |
| Sun sensor board | 2 | 0.42 |
| Command and data handling unit | 1 | 2.17 |
| Battery | 1 | 2.7 |
| Star tracker | 1 | 3.4 |

**Table 2**
The volume of the TSP elements.

| | Dimensions length*width*hight ($cm^3$) | Total volume (cm3) |
|---|---|---|
| PCM cavity (for one cavity) | 6.1 * 1.3 * 1.2 | 9.516 |
| Cover plate | 9.8 * 7.1 * 0.5 | 34.79 |
| Base plate | 9.8 * 7.1 * 0.5 | 34.79 |
| Heat sink walls | 6.1 * 1.2 * 0.5 | 3.66 |
| TSP | 9.8 * 7.1 * 2.2 | 153.07 |

thermophysical properties of all used materials are presented in Table 4.

Four PCM combination cases were investigated, (RT 15 & RT 21), (RT 21 & RT 26), (RT 15 & RT 26), and the triple combination of (RT 15 & RT 21 & RT 26). The PCM was alternatively arranged in the heat sink cavities. For example, for (RT 15 and RT 21) combination, the cavity with digit one, as shown in Fig. 3, was assigned RT 15 material. The adjacent cavity with digit two was assigned RT 21 material, the next

**Table 3**
The weight of the TSP elements for all cases studied.

| | TSP with single PCM cases | | | TSP PCM combination cases | | | |
|---|---|---|---|---|---|---|---|
| Weight (g) | RT 15 case | RT 21 case | RT 26 case | RT 15 & RT 21 case | (RT 21 & RT 26) case | (RT 15 & RT 26) case | (RT 15 & RT 21 & RT 26) case |
| Metal | 265.86 | | | | | | |
| PCM | 50.24 | 50.524 | 50.24 | 50.38 | 50.38 | 50.24 | 50.33 |
| Total | 316.1 | 316.4 | 316.1 | 316.21 | 316.21 | 316.1 | 316.19 |

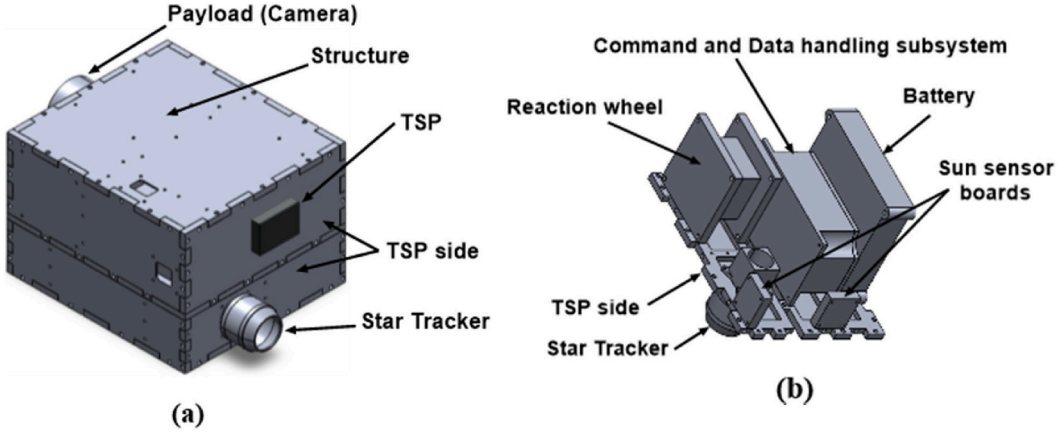


**Fig. 4.** Small satellite dummy model with the proposed TSP mounted on the backside.

**Table 4**
Materials properties [48].

| Materials | | Melting point (°C) | ρ (kg/$m^3$) Solid | $C_p$ (KJ/kg) | K (W/m. K) | LH (KJ/kg) |
|---|---|---|---|---|---|---|
| Phase Change Materials | RT 15 | 15 | 880 | 2000 | 0.2 | 155 |
| | RT 21 | 21 | 885 | 2000 | 0.2 | 155 |
| | RT 26 | 26 | 880 | 2000 | 0.2 | 180 |
| Metals | Aluminium (6061) T6 | _ | 2770 | 897 | 167.9 | _ |

cavity with digit three was assigned RT 15 again, and so on to the end of six cavities. The reason for the PCM distribution in double combination cases was to achieve symmetry in the temperature distribution in the TSP and avoid hot spots due to the difference in melting points. For the triple PCM combination (RT 15 & RT 21 & RT 26), the two middle cavities of digits three and four were assigned RT 15, the cavities with digits two and five were assigned RT 21, and the remaining cavities of digits one and six were assigned RT 26. The lower melting point PCM was localized at the middle of the TSP as the temperature distribution of this location is expected to be the maximum compared to the tips.

The height of the TSP cavity was calculated from the mass of the PCM inside each cavity. Eq. (1). presents a heat balance for the TSP over the entire orbital period. Thus, the required mass of the PCM was distributed equally in each cavity of the TSP. The radiator temperature during the orbital period was assumed to swing around the melting point of the PCM. Consequently, the radiator temperature was averaged during the entire orbital period and equaled the melting point of the PCM.

$$\int_{t=0\ min}^{t=95\ min} \alpha A_s Q_{solar} dt + Q_{load} A_s \Delta t - \varepsilon \sigma A_s T_{melt.}{}^4 \Delta t = m_{pcm}(LH) \quad (1)$$

Where: α is the surface absorbtivity to solar radiation, $Q_{solar}$: is the solar flux, $A_s$: is the cover plate radiator and base plate surface area. $Q_{load}$:is the heat load from the satellite component, $\varepsilon$: is the radiator emissivity to thermal radiation. σ: is the Stefan-Boltzmann constant. $T_{melt.}$:is the PCM melting temperature. LH: is the latent heat of PCM.

## 4. Numerical investigation

A 3-D numerical model of the PCM-based TSP was analyzed using ANSYS fluent 2020 R1 software. The phase transition of the PCM was performed by enabling the melting and solidification model in ANSYS fluent. This model needs essential material properties, such as latent heat value, expansion coefficient, solidus temperature, and liquidus temperature, to capture the phase transition of PCM. In the numerical model, each cavity in the three-dimensional model was treated as a cell zone, a fluid zone. The Thermal storage panel was divided into six separate cavities. Each cavity was isolated from its neighboring one by the separating fins. Therefore, no physical mixing happens between the PCM used.

Small satellites are generally launched to the low earth orbit (LEO). The thermal conditions of the low earth orbit are vastly different from any other orbit. Due to the relatively lower altitude of satellites in LEO, the satellites are subjected to a continuous thermal cycle of heating and cooling as used in our work. The numerical simulations were performed on the TSP in the thermal environment of LEO. The proposed low earth orbit parameters are tabulated in Table 5.

**Table 5**
Parameters of selected orbit.

| Orbit parameter | value |
|---|---|
| Category | LEO |
| Altitude (Km) | 500 |
| Beta angle | 0 Degree |
| Eclipse ratio | 0.368 |
| Eclipse duration (min) | 35 |
| Illumination duration (min) | 60 |

The proposed TSP was supposed to be mounted on one of the small satellite sides where its cover plate faced the outside space while its base plate was attached to the satellite structure. The satellite side on which the TSP was mounted was assumed to be opposite the satellite payload side. The satellite payload was a high-resolution camera that always pointed to the earth by the attitude determination and control subsystem (ADCS). As a result, the TSP side faced the sun during the illumination zone or outer space during the eclipse zone. The problem statement and position of TSP on the satellite in LEO are shown in Fig. 5.

The TSP in the proposed LEO was subjected to a repeated thermal cycle consisting of heating and cooling processes. The former happened when the satellite was between the earth and the sun. That's why this zone is called the illumination zone. While the latter presented when the satellite was in the earth's shadow zone or the eclipse zone. During the heating process, the TSP was subjected to two heat sources, the solar heat flux at its cover plate and the hardware heat load at its base plate. The solar flux lasted for 60 min which is the illumination zone period. While the satellite hardware was in (ON) mode for 20 min. During the cooling process, the hardware was in (OFF) mode, and the TSP radiated its absorbed thermal energy to the outer space. The cooling process lasted for 35 min in the eclipse zone. Three PCM were used in this study, with melting points varying from 15 °C to 26 °C, which are the optimal working temperatures for our case.

To increase the dependency of the results on the melting temperatures of PCM, the materials selected have nearly the same specific heat and hence, the same absorbed sensible heat. In addition, the materials have nearly the same latent heat stored during the heating process. Two case studies were examined. First, the thermal performance of the TSP was investigated using a single PCM in all the heat sink cavities. Secondly, the heat sink cavities were filled with a combination of PCM; thus, the TSP's thermal performance was studied.

The hardware components generate heat during their operation, depending on their efficiency. All these components are powered by electric power from the satellite battery. The more the components' efficiency, the less heat is generated during operation. The adopted hardware heating loads are typical working loads for a satellite project constructed in cooperation between Benha university and the Egyptian space agency. The TSP was designed to be compatible with the satellite's dimensions and weight.

The analysis was performed at two levels of hardware heating loads, 10 W and 13 W. During the illumination zone, the TSP experienced a sinusoidal solar heat flux with a peak solar flux of 1367 $W/m^2$ as shown in Fig. 6. Fig. 6 presents the solar heat flux on the left vertical axis and the structure heat load on the right vertical axis. As the thermal expansion was neglected in this study, densities of the PCM used in the model were fixed and equaled the solid density of PCM mentioned in

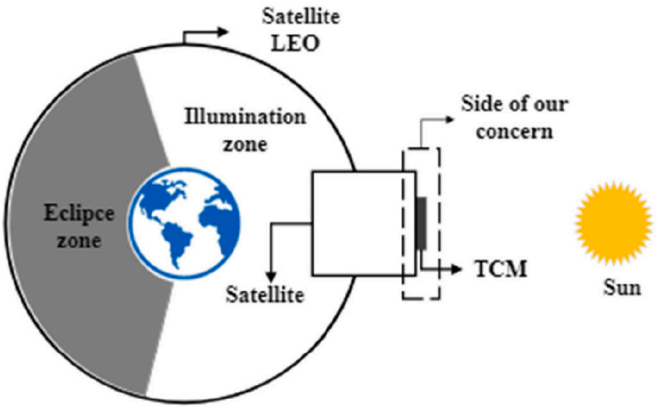


**Fig. 5.** TSP position on satellite and orientation during the proposed LEO.

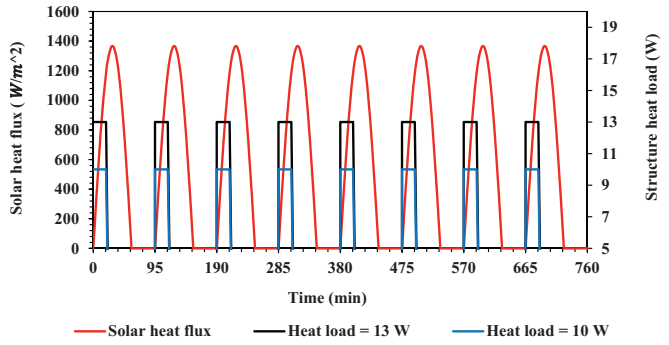


**Fig. 6.** Solar heat flux and hardware heat load during the orbital simulation period.

Table 4.

The following assumptions were adopted in the numerical model to reduce the complexity of the mathematical model.

1. The PCM properties for liquid and solid phases are temperature independent and constant during the simulation.
2. PCM was assumed isotropic, homogeneous, and incompressible.
3. The volume expansion during the phase change of PCM was neglected.
4. The melting temperature range, which is the difference between the liquidus, and solidus temperature, was 1 °C [34,49].
5. The dominant heat transfer mode was conduction, and the natural convection effects of the PCM were neglected [50–52].
6. Convection heat transfer from outside surfaces was neglected due to working in space.

### 4.1. Governing equations

The numerical simulations were performed on a three-dimensional model of the proposed TSP. The finite volume method was used. The phase change process was modeled using the enthalpy-porosity method. In the enthalpy porosity approach, each cell was modeled as a porous zone with a porosity value equal to the liquid fraction in the cell [53,54]. The enthalpy-porosity method considers the latent heat storage by assigning a latent heat value for every computational cell in the energy equation based on the temperature in every cell. When the computational cell undergoes a phase change process, it is modeled as a porous medium with a porosity value equal to the liquid fraction of the PCM inside the cell. The mushy zone constant was set as $10^5$.

The dominant heat transfer mode through the TSP was conduction. Due to working in microgravity conditions, the natural convection effects were neglected, and no need for Navier-Stokes equations. These assumptions could significantly save computational time without influencing the results' reliability. The dominant heat conduction process was modeled using a three-dimensional heat conduction equation, as shown in Eq. (2). The apparent specific heat of the TSP was calculated during the heating process using Eq. (3).

$$\frac{\rho}{k}\frac{\partial(H_S+H_L)}{\partial t}=\frac{\partial^2 T}{\partial x^2}+\frac{\partial^2 T}{\partial y^2}+\frac{\partial^2 T}{\partial z^2} \tag{2}$$

Where, $H_S$: is the sensible enthalpy, $H_L$: is the latent enthalpy. $H_S$ and $H_L$ Assign the total enthalpy H where $H = H_S + H_L$. $\rho$ is the density, and $k$ is the thermal conductivity. For solid domain $H_L$: is always zero, but for the PCM domain, it was considered, and its value was related to the melt fraction in each computational cell.

$$Q_{solar}+Q_{load}-Q_{rad}=m_{TSP}C_{P_{apparent}}(T_{max}-T_i) \tag{3}$$

Where, $Q_s$: is the solar heat, $Q_l$: is the heat load from the satellite hardware components through the structure, $Q_{rad}$: is the outgoing radiation heat to space, $m_{TSP}$: is the mass of the TSP, $C_{p_{app}}$: is the apparent specific heat of the TSP, $T_{max}$:is the maximum temperature reached at the end of a heating process at a steady state, $T_i$: is the initial temperature at the beginning of the heating process. At a steady state, this value varies according to each case.

In the numerical model, a simple scheme was applied for pressure-velocity coupling. But for spatial discretization, PRESTO and second-order upwind methods were used for pressure and energy, respectively. For the energy equation, the convergence criteria were set as $10^{-7}$.

### 4.2. Boundary conditions

The TSP was subjected to heating and cooling processes during the simulation cycle. During the heating process, the TSP was subjected to variable solar heat flux from the top plate and heating load from the satellite hardware components through the structure at the base plate. The illumination zone lasted for 60 min within which a hardware heating load was supplied for the first 20 min. During the cooling process, the TSP radiated thermal radiation to outer space, and the hardware component was in (OFF) mode. The cooling process lasted for 35 min. In addition, the sidewalls were insulated during the entire cycle, and the thermal cycle was repeated several times until the steady state was achieved. The steady state was obtained when the temperature at the end of the orbital period was the same as the temperature at the beginning.

The initial temperature of the solution did not have any impact on the final steady state temperature. Selecting the initial temperature far from the final steady state temperature will only increase the number of solution cycles to obtain steady state results. The initial temperature for each case was selected by expecting the final steady state temperature to decrease the solution time as much as possible. The boundary conditions are summarized as the following according to the proposed coordinate system in Fig. 7.

1. Symmetry boundary conditions

$$\left.\frac{\partial T}{\partial y}\right|_{(x,0,z,t)}=0 \tag{4}$$

2. Heat flux at the base plate.

At $0 \le t < 20$ *min*

$$\dot{Q}_{x,y,0,t}=\dot{Q}_{load} \tag{5}$$

At $20 \le t \le 95$ *min*

$$\dot{Q}_{x,y,0,t}=0 \tag{6}$$

3. Side walls are all insulated

$$\left.\frac{\partial T}{\partial x}\right|_{(0,y,z,t)}=0 \tag{7}$$

$$\left.\frac{\partial T}{\partial x}\right|_{(L,y,z,t)}=0 \tag{8}$$

$$\left.\frac{\partial T}{\partial y}\right|_{(x,w,z,t)}=0 \tag{9}$$

4. Top plate

At $0 \le t < 60$ *min*

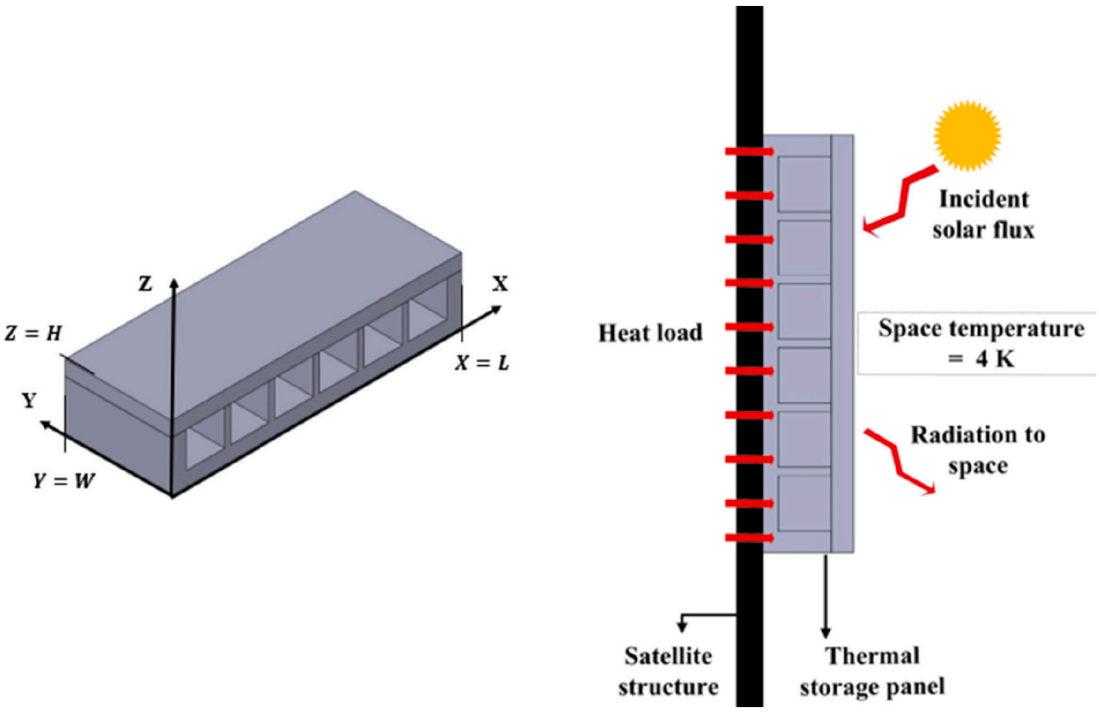


**Fig. 7.** Physical problem boundary conditions and proposed coordinate system.

$$\dot{Q}_{(x,y,H,t)} = \dot{Q}_{solar} - \dot{Q}_{rad.} \tag{10}$$

Where $\dot{Q}_{rad.}$: is the radiation heat transfer to the deep space as Eq. (4).

$$\dot{Q}_{rad} = \varepsilon\sigma A_s\left({T_{surface}}^4 - T_{\infty}^4\right) \tag{11}$$

$T_{surface}$: is the TSP cover plate temperature, $T_{\infty}$: is the deep space temperature 4 K [55,56].

At $60 \leq t \leq 95$ *min*

$$\dot{Q}_{(x,y,H,t)} = -\dot{Q}_{rad.} \tag{12}$$

Fig. 7 presents the boundary conditions of the TSP experiences during the heating process. Two heat loads were subjected to the cover plate, The solar heat flux, and outgoing radiation to the surroundings. In addition, a heat load from the satellite components was applied to the base plate.

### 4.3. Numerical model validation

The present physical problem is a heat transfer problem that includes latent heat storage with heat added and rejected by hardware heating and radiation. The significant physics in our model are the heat conduction and the phase transition phenomenon. The governing equations of these physics are the general conduction equation and the enthalpy porosity method equations, respectively. Both systems of equations were validated with previously reported experimental works. The radiation boundary conditions were also validated along with the general conduction equation and enthalpy porosity method. The mixed radiation and convection boundary conditions were assigned at the external walls of the heat sinks. The radiation boundary conditions were simulated using Stefan-Boltzmann equation. The model validation results concluded that the model could capture well the real amount of radiation heat transfer.

The present numerical model was validated with the formerly experimental work conducted by Mahmoud et al. [31]. In the experimental work, different configurations of finned heat sinks were investigated. The parallel and cross-finned heat sinks were studied at different heat loads of 3 W, 4 W, and 5 W. The parallel fins heat sink had two configurations, 3-cavity, and 6-cavity. At the same time, the cross fins configuration had 9-cavity and 36-cavity. The present numerical model results were validated with the experimental work reported by Mahmoud et al. [31]. The validation was performed with the 6- cavity parallel fins heat sink under heat loads of 3 W and 5 W. Rubitherm RT-42 was used as a PCM whose melting point is 42 °C, while Aluminium T6–6061 was used for the heat sink structure.

The outer dimensions of the heat sink were 50mm in width and length and 25 mm in height. In comparison, the dimensions of each cavity were 6 mm in width, 46 mm in length, and 23 mm in height. The thickness of each fin was 2 mm. The PCM volume adopted in the experimental work by Mahmoud et al. [31] was constant in all heat sink designs and equal to 25 ml which gave a height of PCM in parallel fins 6-cavity heat sink of 15.09 mm. Heat loads of 3 W and 4 W were applied to the cover plate for 60 min. The side walls were set as well insulated. Meanwhile, the top plate was subjected to convection heat transfer to the surrounding with an ambient temperature of 293 K. The heat transfer coefficient was set as 10 $W/m^2K$. The comparison of the transient response between the numerical model and the experimental work by Mahmoud et al. [31] is shown in Fig. 8.

The results show a good agreement between the numerical model results and experimental work results. The numerical model could accurately capture the phase change phenomenon of the PCM. In addition, The numerical model could also accurately predict the base plate temperature value with time. The maximum error obtained between the numerical model and experimental results was 1.9 % and 1.95 % at 3 W and 5 W, respectively.

The present numerical model was also validated independently with the experimental work performed by Yang et al. [51]. The effect of fins configuration on the heat sink thermal performance was investigated in the experimental work. Three fin configurations were studied, with no fins, 1 × 1 cross fins, and 2 × 2 cross fins. At the same time, two PCM were investigated, Octadecanol and *E*-BiInSn, with a constant volume of 100 ml. The heat sink was manufactured with 6063 aluminium alloy with outer dimensions of 80 × 80 × 30 $mm^3$ and inner dimensions of 72 × 72 × 25 $mm^3$ each. The fin thickness in all configurations was 2 mm. A copper block, which was the heat source, with four inserted heating rods

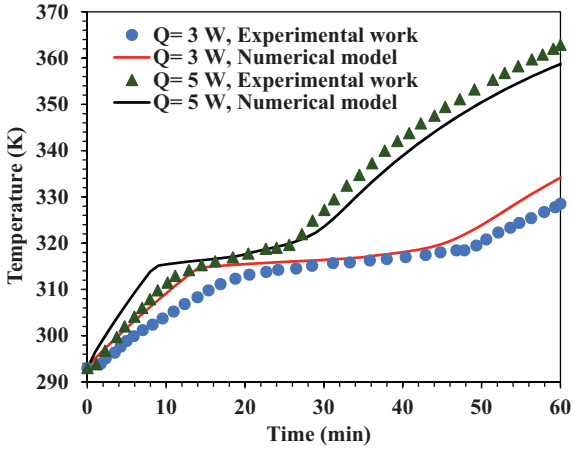


**Fig. 8.** Numerical model validation results with the previously stated experimental work by Mahmoud et al. [31].

and outer dimensions of 60 × 60 × 20 $mm^3$ was attached to the heat sink base plate.

Three heating loads were applied to the heat sink base plate, 80 W, 200 W, and 320 W. The heat load was applied to the heat sink until its base plate temperature reached 140 °C. The numerical model was validated with a 2 × 2 cross fins configuration, including nine cavities under a heat load of 80 W using Octadecanol and E-BiInSn. The heat load was applied to the bottom surface of the copper block. While the side surfaces of the copper block were set as insulation. In addition, the sidewalls of the heat sink and the top surface were exposed to convection heat transfer from the surrounding air with a convective heat transfer coefficient of 10 $W/m^2K$. The initial and ambient temperatures were set at 297 K.

The validation results shown in Fig. 9 revealed a good agreement between the present numerical model results and the experimental work carried out by Yang et al. [51]. As shown in Fig. 9, the base plate temperature is maintained at a nearly constant temperature corresponding to the melting temperature of each material for a considerable amount of time. As a result, the present numerical model describes the phase change phenomenon. The maximum error obtained between the numerical model and the experimental work results is 1.88 %.

To validate the radiation boundary conditions of Stefan-Boltzmann, the present model was validated with a previously reported experimental study by Yamada and Nagano [57]. The experimental work tested a heat storage plate in a thermal vacuum chamber (TVC) under vacuum conditions. The only mode of heat transfer presented in the experimental work was radiation heat transfer. The heat storage plate was made of carbon fiber-reinforced polymers (CFRP) and was filled with eicosane as a PCM. The outer dimensions of the heat storage plate were 15 cm × 15 cm with 2.5 mm thickness. The heat storage plate was attached to an aluminium plate of dimensions 46 cm x 25 cm. A heater with the same dimensions was mounted on the top plane of the heat storage plate. The cycle lasted for 5800 s. The heating cycle was sinusoidal with a peak load of 20 W for 2900 s., and the heater was switched off for the next 2900 s. The heat storage plate was attached to an aluminium plate at the back surface. The heat storage and aluminium plates were covered with (MLI). The tests were performed in a cylindrical thermal vacuum chamber with an outer diameter of 95 cm and a length of 113.5 cm. The TVC shroud temperature was set below −180 °C (93 K), which is the surrounding temperature in the Stefan-Boltzmann equation. The results shown in Fig. 10 obtained a good matching between the experimental and numerical model results. Model parameters and the boundary conditions of the simulation are listed in Table 6. The current numerical model was built using the same validation model setup and solution methods.

### 4.4. Grid and time step independence study

The effect of the grid element number and the value of the transient solution time step was carefully examined for the present model. The mesh was generated using ANSYS meshing feature. Two mesh control methods were used: multizone and body sizing methods. The former was used to generate cell zones with dominant hexagonal elements. At the same time, the latter was used to control the number of elements in the computational domain grid. Grid independence study was performed with RT 15 PCM at 10 W heat load. Four cases of mesh quality at different numbers of elements were examined and were summarized in Table 7. The grid independence test results show a good convergence in the results by increasing the mesh quality. For predicting the peak base plate temperature, the maximum error reported between the coarse and normal mesh was 0.602 %, and between the finer and very fine mesh was 0.19 %.

The results were highly convergent at the very fine mesh. A tradeoff between the numerical error and the computational time was considered for computational time concerns. The finer mesh was considered the best choice for this model solution as the finer mesh provides an acceptable numerical error with a suitable computational time. Fig. 11 shows the computational domain for the PCM and heat sink domains.

A time step independence study was conducted based on the finer mesh quality. Selecting the appropriate time step for capturing the phase change phenomenon is required. Larger time steps may skip the entire

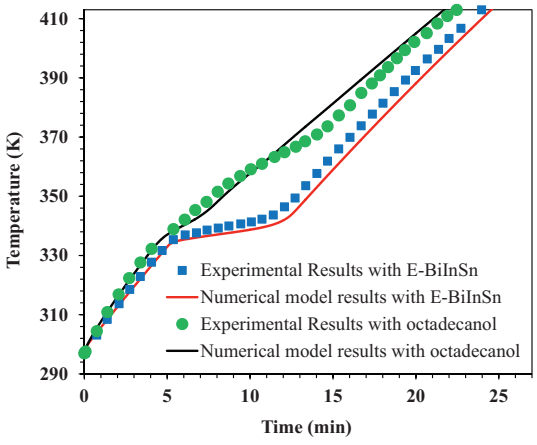


**Fig. 9.** Numerical model validation with the experimental work performed by Yang et al. [51] at heat load 80 W.

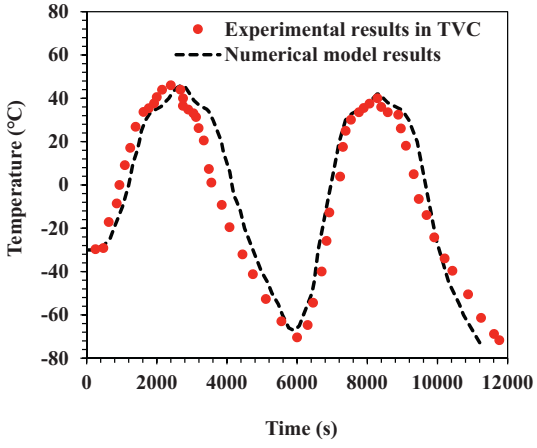


**Fig. 10.** Numerical model validation with the experimental work conducted by Yamada and Nagano [57].

**Table 6**
The validation model parameters.

| Physical parameters | | Models | | Boundary conditions | Initial conditions | Meshing |
|---|---|---|---|---|---|---|
| Body emissivity | 0.82 | 1. Melting and solidification model | | Radiation with Stefan-Boltzmann equation at all boundaries | At time = 0 s. The initial temperature is 243 K | Meshing methods are multizone and mesh sizing (Mesh count is 96,641 element) |
| Plate heater load | 20 W | 2. Energy equation | | | | |
| TVC shroud temperature | 93 K | Mushy zone constant | $10^5$ | | | |
| $\rho_{CFRP}$ | 1800 kg/m$^3$ | pressure discretization | PRESTO | | | |
| $K_{CFRP}$ | 347 W/m K | pressure-velocity coupling | simple scheme | | | |
| $C_{p\ (CFRP)}$ | 700 J/kg. K | energy discretization | second order upwind | | | |

**Table 7**
The grid and time step independence study.

| Grid independence study | | | | | Time step independence study | |
|---|---|---|---|---|---|---|
| Mesh quality | No. of elements | | Temperature | | Time step (s) | Base plate maximum temperature (°C) |
| | PCM zone | Metal zone | the peak of the base plate temperature (°C) | At the end of the orbital period (°C) | | |
| Course | 3621 | 6086 | 21.58 | 7.15 | 5 | 21.37 |
| Normal | 8619 | 14,506 | 21.45 | 7.67 | 1 | 21.13 |
| Finer | 28,928 | 48,688 | 21.37 | 7.84 | | |
| Very fine | 222,917 | 375,187 | 21.33 | 7.92 | 0.1 | 21.15 |

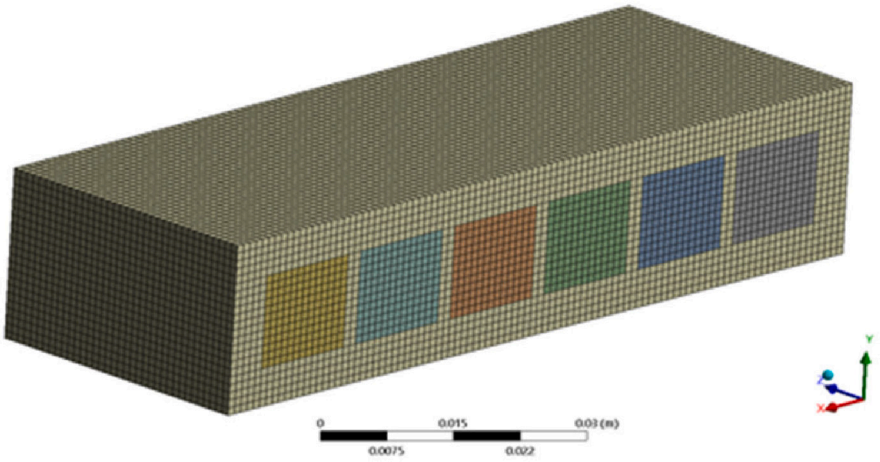


**Fig. 11.** The grid of the computational domain at finer mesh quality.

phase change phenomenon. The time steps presented in Table 7 are the maximum values of time steps adopted by the solver. The solver may consider lesser values to achieve the convergence criteria. The time step independence test revealed no significant change in the base plate maximum temperature as the time step varied from 5 to 0.1 s. Thus, 5 s time step was adopted to account for the computational time and cost considerations.

## 5. Results and discussions

In this item, the transient simulation results are discussed and analyzed. Section 5.1. presents the transient simulation results for the base plate temperature of the heat sink for single and PCM combination cases. While section 5.2. discusses the results of temperature and liquid fraction contours. Also, Section 5.3. presents and discusses the results of a critical time when the TSP temperature was outside the recommended range. Section 5.4 discusses the peak temperature differences. Finally, Section 5.5. presents the results of the apparent heat capacity for the different cases performed in this study.

### 5.1. Base plate temperature

In the first analysis stage, the heat sink was filled with a single PCM with melting temperatures of 15 °C, 21 °C, and 26 °C. The base plate temperature is a significant parameter in evaluating the thermal performance of the TSP during the transient simulations. The base plate temperature provides information about the satellite hardware surface temperature, which is an issue of our concern. Thus, the area average of the base plate temperature is presented at the base plate of the heat sink. The model was subjected to several thermal cycles until a steady state was obtained. The temperature results show the harmonic response of base plate temperature during the orbital period. Figs. 12 and 13 show the heat sink's base plate temperature when the heat sink was filled with a single PCM at heating loads of 10 W and 13 W. At 10 W, the initial temperatures for all cases were 22 °C, 2 °C, −1 °C, and − 3 °C for the case without PCM, RT 15, RT 21, and RT 26, respectively. At the same time, the initial temperatures were 0 °C for the case without PCM, RT 15, and RT 26 at 13 W heating load. The initial temperature was 7 °C for RT 21 at a 13 W heating load.

At steady state, the temperature was swinging between the minimum

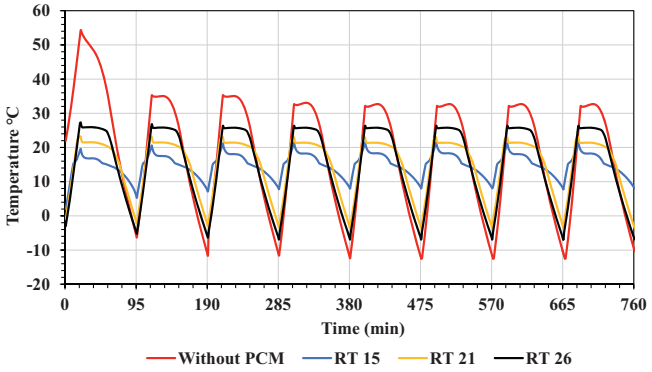


**Fig. 12.** Base plate temperature during the transient analysis of a single PCM-filled heat sink at a heating load Q = 10 W.

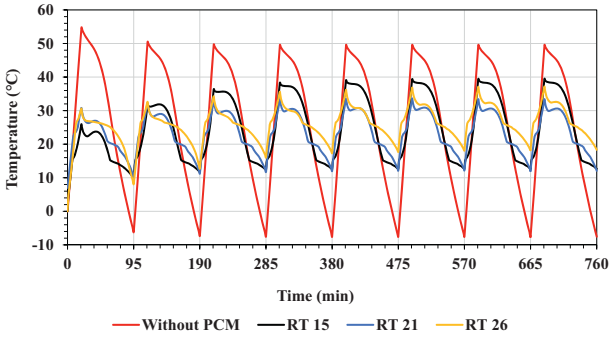


**Fig. 13.** Base plate temperature during the transient analysis of a single PCM-filled heat sink at a heating load Q = 13 W.

and maximum extrema points. At the beginning of the illumination zone, the base plate temperature was below the melting temperature of the PCM. Hence, the PCM stored SH, and thus, its temperature increased, as shown in Fig. 12. When the temperature reached the melting temperature of the PCM, the melting process began, and the PCM started to store the heat in the form of LH. During the melting process, the temperature remained constant for a considerable period. Fig. 12 shows the effect of integrating PCM within the TSP. The case without PCM, in which only radiators are integrated on the TSP outer surface, recorded the highest maximum extrema and the lowest minimum extrema of 32.7 °C and − 12.5 °C, respectively. PCM could significantly decrease the maximum extrema and increase the minimum extrema. RT 15 recorded the lowest maximum extrema of 21.4 °C with a decreasing percentage of 34.6 % compared to the case without PCM. In addition, RT 15 recorded minimum extrema of 7.8 °C, increasing by 162.4 %. At the same time, RT 21 recorded maxima and minima extrema of 23 °C and − 3.5 °C, respectively. While RT 26 obtained maxima and minima extrema of 26.3 °C and − 6.8 °C, respectively. The minimum melting point PCM recorded better thermal performance than the intermediate and higher melting point PCM.

Fig. 13 shows the temperature profile of the transient simulations for a single PCM-filled TSP at a heating load of 13 W. The case without PCM recorded extreme temperature values outside the recommended temperature range. At steady state, the maximum and minimum extrema temperatures were 49.5 °C and − 7.5 °C, respectively. However, the PCM-based TSP recorded a significant reduction in the maximum extrema and an increase in the minimum extrema. RT 15 recorded maximum and minimum extrema of 39.5 °C and 12.6 °C, respectively. RT 15 could decrease the maximum extrema temperature by 20.2 % and increase the minimum extrema by 268 %. However, the maximum extrema decreased by 25 % and 32.52 % at RT 26 and 21, respectively. In addition, the increase in minimum extrema was 343.6 % and 258.9 % at RT 26 and 21, respectively.

Figs. 14 and 15 present the temperature results during the transient and steady state when the TSP was filled with multiple PCM at 10 W and 13 W, respectively. Four cases were investigated, (RT 15 & RT 21), (RT 21 & RT 26), (RT 15 & RT 26), and (RT 15 & RT 21 & RT 26). Each case was investigated under heating loads of 10 W and 13 W. At 10 W, the initial temperatures adopted are 22 °C, −1 °C, 7 °C,7 °C, and − 2 °C for cases without PCM, (RT 15 & RT 21), (RT 21 & RT 26), (RT 15 & RT 26), and (RT 15 & RT 21 & RT 26), respectively. In contrast, at 13 W, the initial temperatures adopted are 0 °C, 0 °C, 7 °C, 9 °C, and 7 °C for cases without PCM, (RT 15 & RT 21), (RT 21 & RT 26), (RT 15 & RT 26), and (RT 15 & RT 21 & RT 26), respectively.

Fig. 14 shows that the PCM combination could significantly reduce the maximum extrema and increase the minimum extrema. It was remarked that the temperature results for PCM combination cases were averaged between the results of the individual single PCM. The combination of (RT 15 & RT 21) recorded maximum and minimum extrema of 22.5 °C and − 6.5 °C with a reduction and increase percentages of 31.1 % and 94.78 %, respectively. A significant remark was observed from the results, the dependency of the base plate temperature with PCM melting point was significantly decreased for PCM combinations. The maximum variation in maximum extrema was 3.2 °C between (RT 15 & RT 21) and (RT 21 and RT 26) combinations. However, the maximum variation in minimum extrema was 3 °C between (RT 15 & RT 26) and (RT 15 & RT 21) combinations.

Fig. 15 shows the temperature response for PCM combinations under a heating load of 13 W. The triple PCM combination (RT 15 & RT 21 & RT 26) recorded the lowest maximum extrema and could lower it from 49.5 °C in the case without PCM to 35 °C with a reduction percentage of 29.36 %. In addition, the triple PCM combination could increase the minimum extrema by 244 %. The case without PCM recorded minimum extrema of −7.55 °C. (RT 21 & RT 26) combination recorded the highest minimum extrema of 17.22 °C. with an increasing percentage of 328 %.

### 5.2. *Temperature and liquid fraction contours*

The liquid fraction results were analyzed and reported during the transient thermal analysis of the TSP for all cases. Figs. 16 and 17 present the liquid fraction contours for (RT 15 & RT 26) PCM combination at a heating load of 10 W, and 13 W, respectively. At the beginning of the illumination zone (Heating process), the heat sink temperature increased until it reached the melting point of RT 15; then, RT 15 experienced a melting process while RT 26 was still in the solid phase. Once the heat sink temperature reached the melting point of RT 26, its melting process started. Fig. 16 shows that RT 26 could not melt during the illumination zone (heating process). Thus, its phase was stuck to a solid phase during both the illumination and eclipse zones. The explanation was that the temperature of the TSP did not reach the melting temperature of RT 26 (26 °C) during the heating process. Thus, RT 26

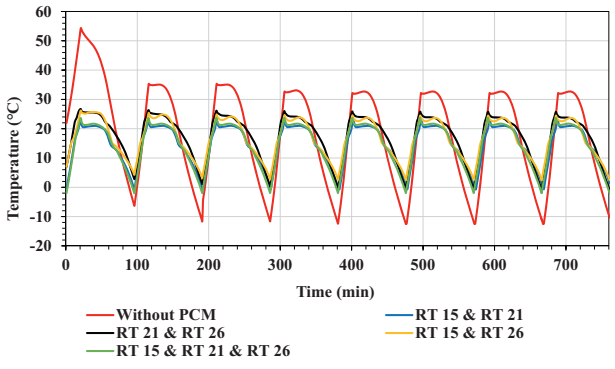


**Fig. 14.** Base plate temperature during the transient analysis of multiple PCM-filled heat sink at a heating load of 10 W.

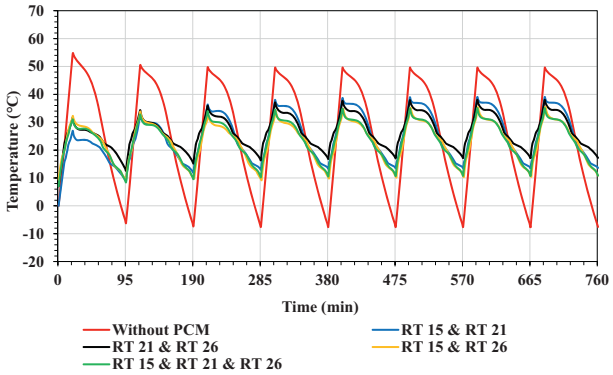


**Fig. 15.** Base plate temperature during the transient analysis of multiple PCM-filled heat sink at a heating load of 13 W.

could not melt and remained in a solid state.

It is evident from Figs. 16 and 17 that PCM's solidification and melting processes started from the cavities' boundary and then traveled through the entire PCM volume. In Fig. 16, At 13 W heating load, RT 26 was activated, and a liquid fraction of unity was recorded at the end of the heating process. At the higher heating load, the temperature of the TSP exceeded the melting temperature of RT 26. Hence, RT 26 experienced a melting process during heating until it was completely melted at the end of the heating process.

Fig. 18 shows the temperature contours for the RT 15 & RT 26 combination case at 10 W heating load during the entire orbital period at a steady state. The heat sink structure material had a thermal conductivity significantly higher than the thermal conductivity of PCM. Regardless of the temperature gradient between the cover plate and the bottom plate at the beginning of the heating and cooling processes, the temperature distribution was nearly uniform in the heat sink structure metal, unlike the temperature distribution in the PCM domain. As shown in Fig. 18, the heat sink temperature increased during the heating zone until the temperature reached the maximum extrema. The temperature declined again to reach the same temperature at the beginning of the heating process.

Generally, in PCM combination cases, each fin in the heat sink was neighboring two different PCM. One side of the fin was in contact with a higher melting point PCM, and the other was with a lower melting point PCM. So, an interesting phenomenon was observed from the temperature contours. The observations showed a temperature gradient between the fins' sides for PCM combination cases when one of the neighboring PCM was subjected to a phase change process (melting or solidification). Fig. 19 illustrates the temperature gradient across the fins for RT 15 & RT 26 combination for 13 W heating load at 5 min.

The explanation of such phenomenon was outlined. At the beginning of the heating process, the temperature was the same throughout the entire domain of the TSP. The PCM around each fin has a different melting temperature. Therefore, the one with the lower melting point underwent a melting process before the one with the higher melting temperature. During the phase transition of the lower melting point PCM, its temperature was nearly constant, while the other PCM with the higher melting point was still in the solid phase, and its temperature was rising. This distinction resulted in one PCM on one side of a fin having a constant temperature during heating and the other PCM on the other side of the fin experiencing an increase in temperature. Therefore, a temperature gradient across the fin sides was observed during the phase transition process. The temperature gradient was observed not only during the heating process but also during the solidification process while cooling.

### 5.3. Critical time results

The temperature of the TSP at higher and significantly higher heating loads were observed to exceed the recommended operating temperature range of the satellite hardware. In this subsection, the duration for which the TSP was exposed to temperature values outside the recommended temperature range at heating loads of 13 W was obtained. The critical temperature adopted was 30 °C. The duration for which the component temperature exceeded the prescribed critical temperature was reported.

Fig. 20 presents the duration of exposure to extreme temperature values for all cases at heating loads of 13 W. It was observed that PCM with lower melting points recorded lower time durations for single PCM cases. For the case without PCM, the extreme time duration was 45.4 min. For single PCM cases at 13 W heat load, RT 21 recorded the minimum time duration of 15 min with a reduction percentage of 66.9 %. While RT 15 recorded a maximum time duration of 40.9 min with a reduction percentage of 9.9 %. For PCM combination cases, the critical time durations were lower than the durations of the case without PCM. The triple PCM combination recorded the lowest extreme time duration among PCM combination cases. The triple combination achieved 29.5

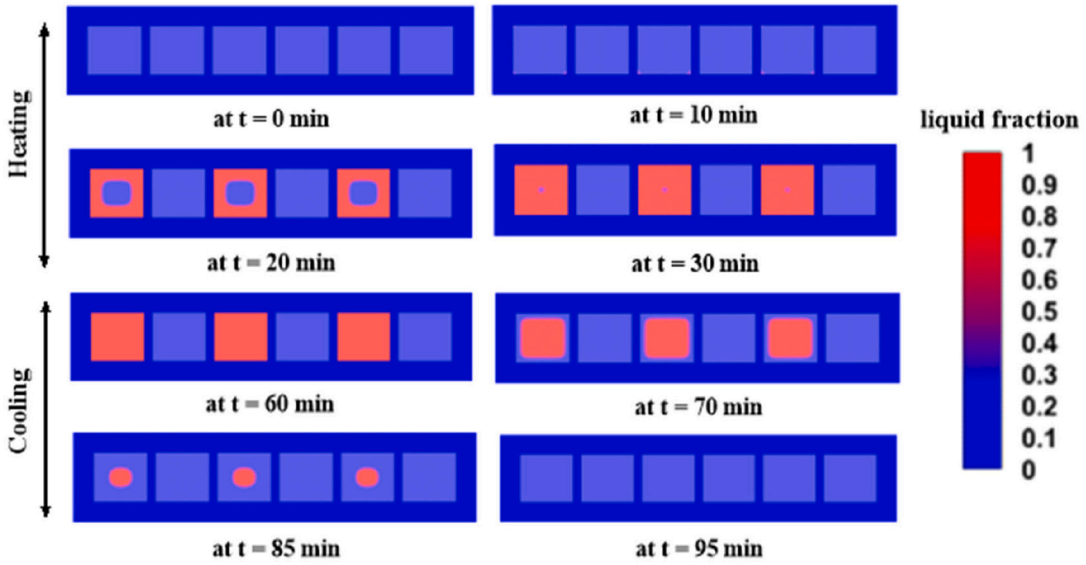


**Fig. 16.** Liquid fraction contours of RT 15 & RT 26 PCM combination at 10 W.

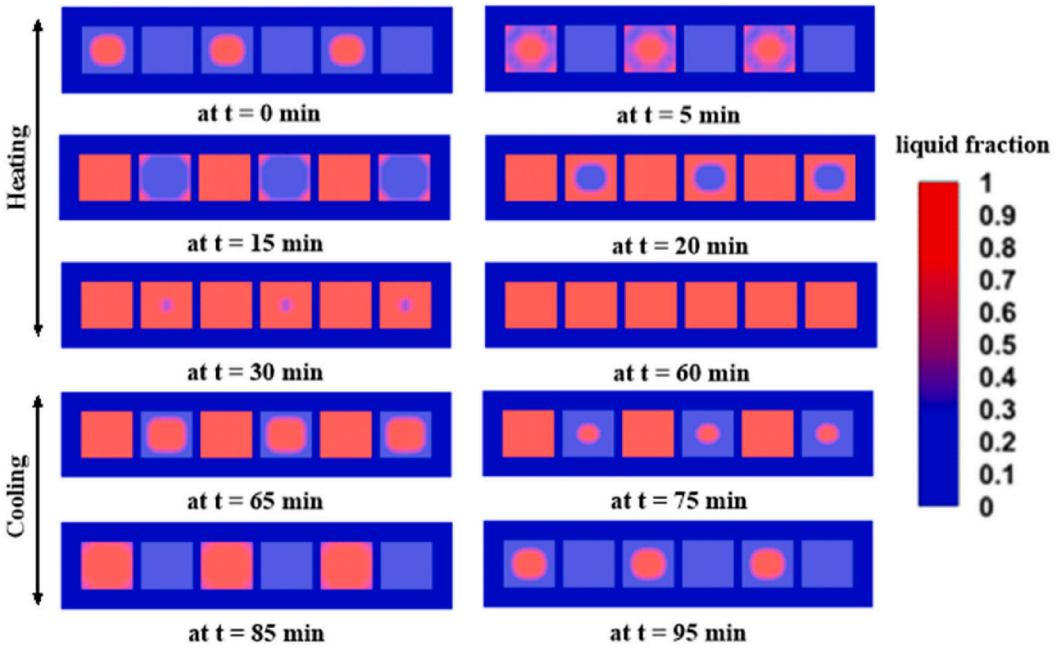


**Fig. 17.** Liquid fraction contours of RT 15 & RT 26 PCM combination at 13 W.

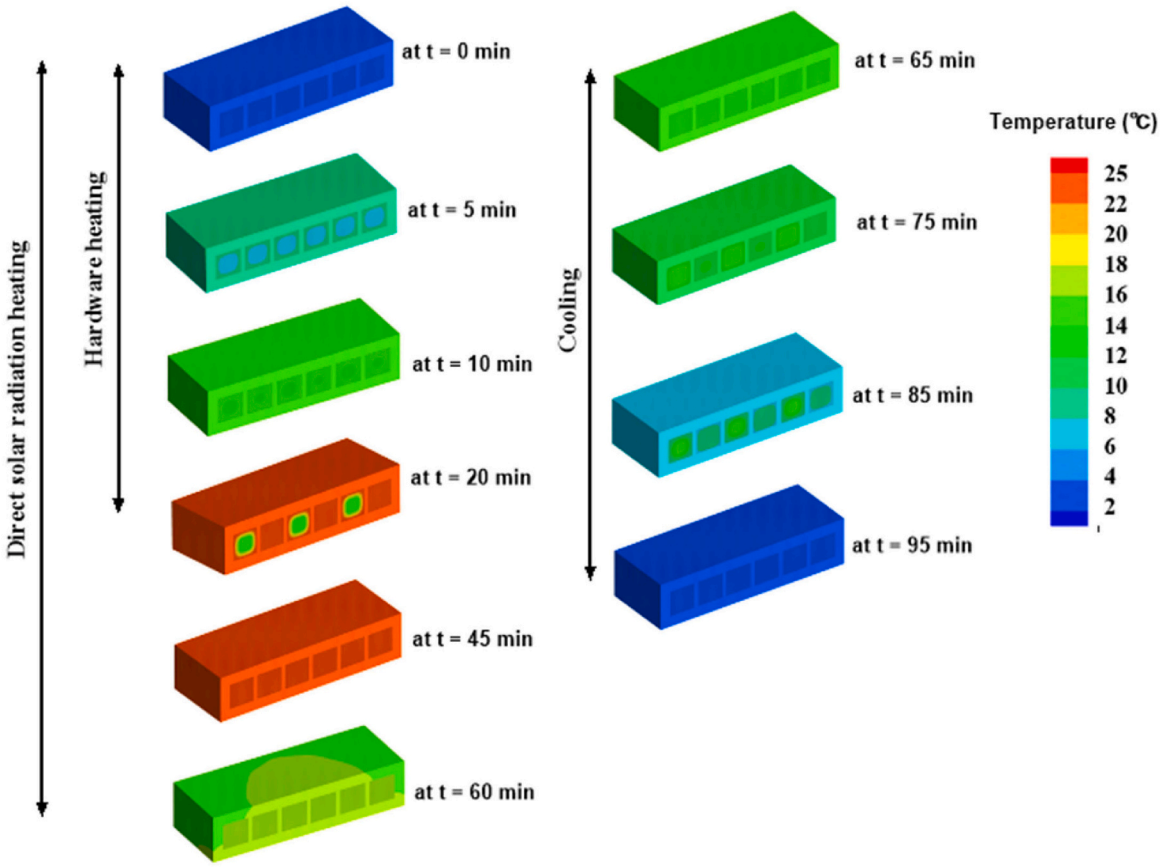


**Fig. 18.** Temperature contours of RT 15 & RT 26 PCM combination at 10 W during the entire orbital period.

min critical time with a reduction percentage of 35 %. (RT 15 & RT 26) PCM combination recorded an extreme time duration of 29.74 min, while (RT 21 & RT 26) recorded 38.8 min with reduction percentages of 34.5 % and 14.5 %, respectively. In addition, (RT 15 & RT 21) combination recorded 41.3 min extreme time duration with a reduction percentage of 9 %.

### *5.4. Peak temperatures difference (PTD)*

Peak temperatures difference (PTD) was a significant parameter

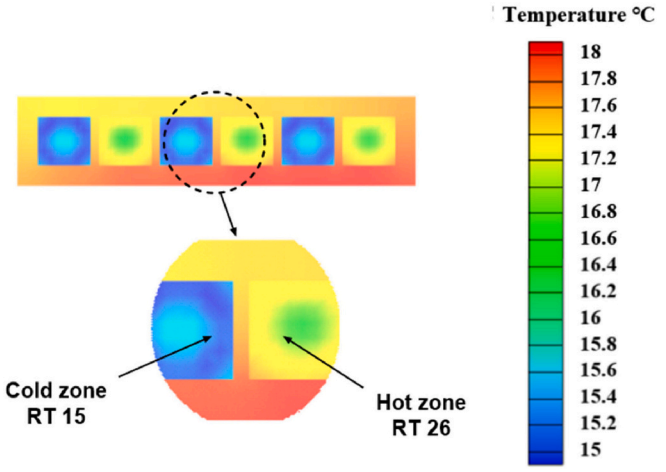


**Fig. 19.** Scheme for Temperature gradient illustration across the fins for RT 15 & RT 26 combination at 13 W and $t = 5$ min.

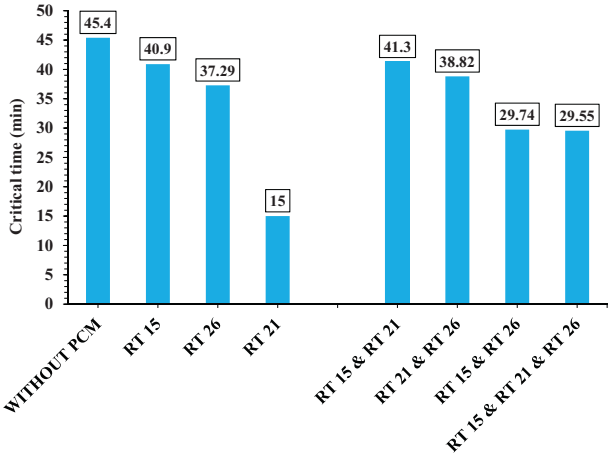


**Fig. 20.** The critical exposure time to extreme temperature values outside the recommended range at 13 W heating load.

adopted for analyzing the solution results and the TSP thermal performance. PTD refers to the difference between the maximum and minimum extrema temperature at steady state. The harmonic response of satellite components' temperature is not preferable and should be reduced as possible. PTD is equivalent to twice the temperature amplitude at steady state condition. The higher the PTD lower the thermal performance of the TSP and vice versa. Figs. 21 and 22 present the PTD for single PCM and PCM combination cases, respectively. The case without PCM presented the highest PTD among other cases of 45.2 °C and 57.1 °C at 10 W and 13 W, respectively.

As shown in Figs. 21 and 22, the cases with PCM achieved a significant decrease in PTD. For single PCM cases, as shown in Fig. 19, RT 15 achieved a PTD of 13.5 °C and 26.8 °C at 10 W and 13 W with a reduction percentage of 70.13 % and 113 %, respectively. At 13 W, RT 26 could reduce the PTD by about 66.8 %. Significant criteria for thermal performance evaluation are presented in Fig. 21 and Fig. 22. The change in PTD with changing the heating load is significant. The heating load from the satellite structure is highly probable due to the intermittent operation of satellite components and subsystems. The vertical side of the dashed line box prescribed in Fig. 21 and Fig. 22 indicates the change in PTD with the change in heating load.

As shown in Fig. 22, the PCM combination presented significant stability in the PTD and fixed the temperature margins of satellite components with heating load alteration. The combination of (RT 15 &

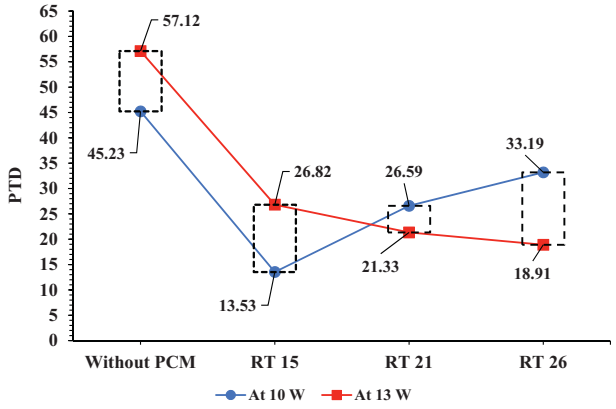


**Fig. 21.** Peak temperatures differences for single PCM cases.

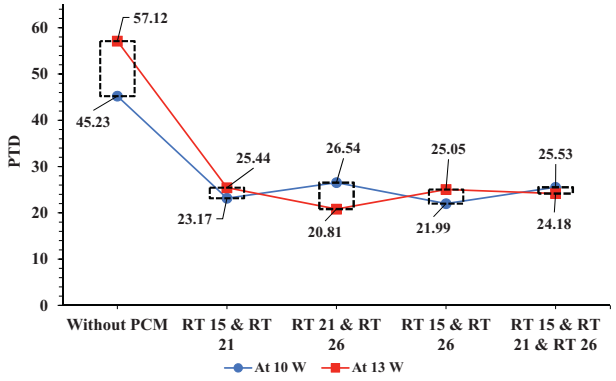


**Fig. 22.** Peak temperatures difference for PCM combination cases.

RT 21) could reduce the PTD range by 82.9 % relative to the single RT 15 and 56.8 % relative to the single RT 21. The triple PCM combination reported the higher reduction in PTD range. The combination of (RT 15 & RT 21 & RT 26) reported a reduction in PTD range by 89.84 %, 74.3 %, and 90.5 % at single RT 15, RT 21, and RT 26, respectively. It was remarked that combining the intermediate melting point PCM (RT 21) with the higher melting point PCM could not impose any significance in decreasing the PTD range relative to the single RT 21. As discussed in Fig. 14 and Fig. 15, the PCM melting point significantly affected the base plate temperature. PCM combination had more than one melting point, so they had combined effects and resulted in more stability in the swinging temperature response and the PTD.

### 5.5. *Apparent specific heat*

The apparent specific heat of the TSP during the heating process was calculated using Eq. (3). Fig. 23 shows the apparent specific heat for single PCM cases, while Fig. 24 shows the results for PCM combination cases. For Fig. 23, At the heating load of 10 W, the lower melting point PCM achieved a lower base plate maximum temperature. Therefore, they achieved higher apparent specific heat values. In addition, PCM with higher melting points achieved higher base plate maximum temperature. Hence lower values of apparent specific heat. At 10 W, in the case without PCM, the specific heat was 2.63 Kj/kg. K. On the one hand, RT 15 achieved the highest value of 7.42 Kj/kg. K, with an increase of 182.13 % compared to the case without PCM. On the other hand, RT 26 recorded the lowest value of specific heat, among PCM cases, of 3 Kj/kg. K, with an increase of 14 % compared to the case without PCM.

For PCM combinations, as shown in Fig. 24, (RT 15 & RT 26) combination recorded a specific heat of 4.57 Kj/kg. K for both 10 W and 13 W, with an increasing percentage of 73.7 %. The specific heat values did

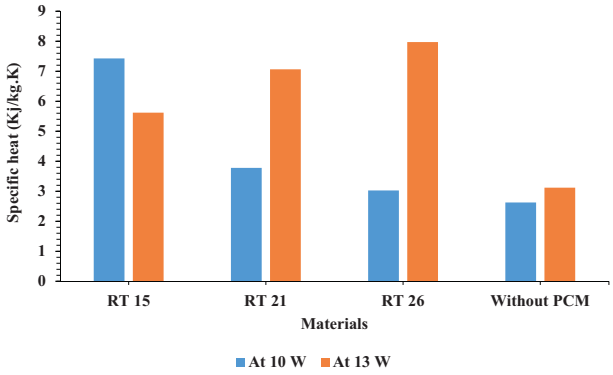


**Fig. 23.** Apparent specific heat of single PCM cases for the heating process.

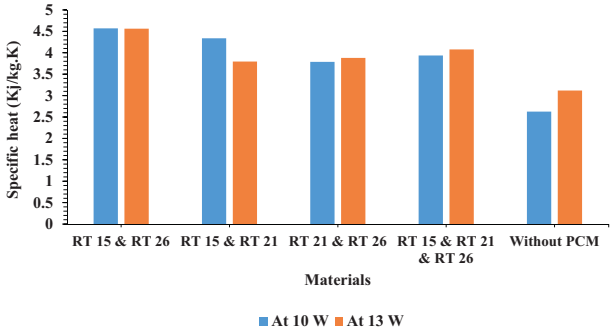


**Fig. 24.** Apparent specific heat of single PCM combination cases for the heating process.

not change remarkably with the change in the heating load for the PCM combination. (RT 15 & RT 21) achieved a specific heat of 4.3 and 3.8 Kj/kg. K at 10 W and 13 W, respectively. While (RT 21 & RT 26) combination achieved specific heat of 3.8 and 3.9 Kj/kg. K at 10 W and 13 W, respectively. The triple combination recorded specific heats at 10 W and 13 W of 3.9 and 4 Kj/kg. K, respectively. It was concluded from Fig. 24 that the PCM combination had stable thermal storage effectiveness with a varying heating load.

## 6. Conclusion

This work presents a transient three-dimensional numerical thermal analysis of a thermal storage panel (TSP) for thermal control of satellites in low earth orbit. The effect of phase change materials (PCM) melting point and PCM combination on the thermal performance of the TSP was investigated. The TSP was designed based on a typical small satellite configuration. The thermal performance of the TSP was analyzed under the thermal conditions of a low earth orbit (LEO). The TSP was an aluminium heat sink integrated with five internal fins. The internal fins divided the interior of the heat sink into six cuboid cavities, which contained the PCM and prevented their mixing. The fins were also a thermal conductivity enhancer to overcome PCM's relatively low thermal conductivity. The study revealed significant conclusions, which are outlined in the following.

- PCM encapsulation inside an aluminium heat sink with high thermal conductivity effectively increases the PCM's low thermal conductivity.
- Small satellites' intermittent thermal environment in space imposes difficulties in designing thermal control subsystems. PCM is a promising solution for the thermal controllability problems of small satellites. PCM can significantly increase the thermal control performance of satellites by raising its thermal storage capabilities without a remarkable increase in satellite mass.
- PCM-based TSP significantly improves thermal control performance by storing the heat energy during the illumination zone and repelling it to the satellite components during the eclipse zone, avoiding overheating or overcooling.
- PCM melting point is a dominant factor that considerably influences the thermal performance of the PCM - based TSP under a time-dependent thermal environment like the LEO thermal environment.
- The PCM with the intermediate melting point, relative to our application, presented the best thermal performance at the temperature and critical time level.
- The PCM combination could not have a remarkable effect on the critical time. Instead, The PCM combination shows significant stability in the temperature response amplitude under varying heating loads. In addition, the specific heat, which reflects the thermal storage ability, was nearly constant for PCM combination cases under different heating loads.
- The effective PCM combinations which resulted in good impact were the combination of lower melting point with the higher melting point PCM, the lower melting point with the intermediate melting point PCM, and the triple PCM combination. The combination of intermediate melting point with the higher melting point PCM could not impose any remarkable effect.
- PCM combination resulted in a significant phenomenon of a temperature gradient across the thin partitioning fins, which separated the PCM in the heat sink and prevented mixing between them. This phenomenon was remarked during the phase transition of one PCM in the combination.
- Future research should be dedicated to studying the effect of this temperature gradient on the TSP from the thermal stress perspective and the ways to reduce this temperature gradient by novel PCM partitioning designs.

## Author statement

Persons who meet authorship criteria are listed as authors, and all authors certify that they have participated sufficiently in the work to take public responsibility for the content, including participation in the concept, design, analysis, writing, or revision of the manuscript. Furthermore, each author certifies that this material or similar material has not been and will not be submitted to or published in any other publication before its appearance in the journal of energy storage.

## Authorship contributions

Mr. Abdelrahman Elshaer: He is a M.Sc. student. He did most of the work of building the model, conducting the findings, drawing the results and writing the first version of the paper.

Dr. Ahmed Antar Hawwash: He helped the student to build the numerical model and revise the results.

Prof. Aref Soliman: He is the major supervisor of the work and he checked most of the work like the model, the results, and proofread the work.

Dr. Mohamed Kassab: He helped the student in drawing the results and discussing it with the team. He also helped the team in using the software adopted in the work.

## Declaration of Competing Interest

We disclose any actual or potential conflict of interest including any financial, personal or other relationships with other people or organizations within three years of beginning the submitted work that could inappropriately influence, or be perceived to influence, this work.

## Data availability

Data will be made available on request.

## Acknowledgment

It is a great pleasure to highly acknowledge the Egyptian Space Agency for their financial and technical support in carrying out the present work.

## References

[1] T. Liu, Q. Sun, J. Meng, Z. Pan, Y. Tang, Degradation modeling of satellite thermal control coatings in a low earth orbit environment, Sol. Energy 139 (2016) 467–474, https://doi.org/10.1016/j.solener.2016.10.031.
[2] C.H. Wang, J.Der Huang, C.R. Chen, Numerical study on the thermal control of the TriG receiver for FORMOSAT-7 satellite, Procedia Eng 79 (1) (2014) 279–288, https://doi.org/10.1016/j.proeng.2014.06.344. ICM.
[3] A.A. Hawwash, H. Hassan, K. el Feky, Impact of reactor design on the thermal energy storage of thermochemical materials, Appl. Therm. Eng 168 (2020), https://doi.org/10.1016/j.applthermaleng.2019.114776.
[4] A.A. Hawwash, H. Hassan, M. Ahmed, S. Ookawara, K. el Feky, Long-term thermal energy storage using thermochemical materials, Energy Procedia 141 (2017) 310–314, https://doi.org/10.1016/j.egypro.2017.11.111.
[5] A.A. Hawwash, S. Mori, K. el Feky, H. Hassan, Numerical study for open reactor design using salt hydrate, IOP Conference Series: Earth and Environmental Science 322 (1) (2019), https://doi.org/10.1088/1755-1315/322/1/012021.
[6] G.P. Peterson, Thermal Control Systems for Spacecraft Instrumentation 24, AIAA Paper, 1983, https://doi.org/10.2514/6.1983-1491 no. 1.
[7] D. Gilmore, Spacecraft Thermal Control Handbook Second edi, I, 2002.
[8] K. Azzouz, D. Leducq, D. Gobin, Enhancing the performance of household refrigerators with latent heat storage: an experimental investigation, Int. J. Refrig. 32 (7) (2009) 1634–1644, https://doi.org/10.1016/j.ijrefrig.2009.03.012.
[9] R. Elarem, S. Mellouli, E. Abhilash, A. Jemni, Performance analysis of a household refrigerator integrating a PCM heat exchanger, Appl. Therm. Eng. 125 (2017) 1320–1333, https://doi.org/10.1016/j.applthermaleng.2017.07.113.
[10] K. Yamada, H. Nagano, Development of a heat storage panel for micro/nano-satellites and demonstration in orbit, Appl. Therm. Eng. 91 (2015) (2015) 894–900, https://doi.org/10.1016/j.applthermaleng.2015.08.073.
[11] R.F. Coker, Thermal modeling in support of the edison demonstration of smallsat networks project, in: 43rd International Conference on Environmental Systems, 2013, https://doi.org/10.2514/6.2013-3368.
[12] S. Madruga, C. Mendoza, Heat transfer performance and thermal energy storage in nano-enhanced phase change materials driven by thermocapillarity, Int. Commun. Heat Mass Transfer 129 (2021), https://doi.org/10.1016/j.icheatmasstransfer.2021.105672.
[13] S. Madruga, C. Mendoza, Enhancement of heat transfer rate on phase change materials with thermocapillary flows, Eur. Phys. J. Spec. Top. 226 (6) (2017) 1169–1176, https://doi.org/10.1140/epjst/e2016-60207-7.
[14] T.D. Swanson, G.C. Birur, NASA thermal control technologies for robotic spacecraft, Applied Thermal Engineering 23 (9) (2003) 1055–1065, https://doi.org/10.1016/S1359-4311(03)00036-X. SPEC.
[15] M. Giangi, F. Stella, E. Leonardi, G. de Vahl Davis, A numerical study of solidification in the presence of a free surface under microgravity conditions, Numer. Heat Transfer, Part A 41 (6–7) (2002) 579–595, https://doi.org/10.1080/104077802317418223.
[16] K.N. Shukla, Heat pipe for aerospace applications—an overview, J. Electron. Cool. Therm. Control 05 (01) (2015) 1–14, https://doi.org/10.4236/jectc.2015.51001.
[17] M.T. Ababneh, C. Tarau, W.G. Anderson, J.T. Farmer, Thermal control of lunar and mars rovers/landers using hybrid heat pipes, J. Thermophys. Heat Transfer 33 (3) (2019) 705–713, https://doi.org/10.2514/1.T5590.
[18] S. Madruga, C. Mendoza, Scaling laws during melting driven by thermocapillarity, Int. J. Heat Mass Transf. 163 (2020), https://doi.org/10.1016/j.ijheatmasstransfer.2020.120462.
[19] M.N.A. Hawlader, M.S. Uddin, M. Khin, Microencapsulated PCM thermal-energy storage system, Available: www.elsevier.com/locate/apenergy.
[20] P.B. Salunkhe, P.S. Shembekar, A review on effect of phase change material encapsulation on the thermal performance of a system, Renew. Sust. Energ. Rev. 16 (8) (2012) 5603–5616, https://doi.org/10.1016/j.rser.2012.05.037.
[21] S.W. Hansen, et al., Water-based phase change material heat exchanger development, in: 44th International Conference on Environmental Systems, 2014.
[22] W.C.G. Humphries, Performance of Finned Thermal Capacitors, 1974.
[23] A. Abhat, M. Groll, Investigation of Phase Change Material /PCM/Devices for Thermal Control Purposes in Satellites, 1974, https://doi.org/10.2514/6.1974-728.
[24] M. Gottero, et al., Phase-change thermal capacitors for ExoMars 2016 mission, in: 44th International Conference on Environmental Systems, 2014, pp. 1–15.
[25] R. Baby, C. Balaji, Experimental investigations on phase change material based finned heat sinks for electronic equipment cooling, Int. J. Heat Mass Transf. 55 (5–6) (2012) 1642–1649, https://doi.org/10.1016/j.ijheatmasstransfer.2011.11.020.
[26] R. Baby, C. Balaji, Thermal optimization of PCM based pin fin heat sinks: an experimental study, Appl. Therm. Eng. 54 (1) (2013) 65–77, https://doi.org/10.1016/j.applthermaleng.2012.10.056.
[27] S. Madruga, C. Mendoza, Introducing a new concept for enhanced micro-energy harvesting of thermal fluctuations through the marangoni effect, Appl. Energy 306 (2022), https://doi.org/10.1016/j.apenergy.2021.117966.
[28] W.F. Wu, N. Liu, W.L. Cheng, Y. Liu, Study on the effect of shape-stabilized phase change materials on spacecraft thermal control in extreme thermal environment, Energy Convers. Manag. 69 (2013) 174–180, https://doi.org/10.1016/j.enconman.2013.01.025.
[29] T.Y. Kim, B.S. Hyun, J.J. Lee, J. Rhee, Numerical study of the spacecraft thermal control hardware combining solid-liquid phase change material and a heat pipe, Aerosp. Sci. Technol. 27 (1) (2013) 10–16, https://doi.org/10.1016/j.ast.2012.05.007.
[30] W.L. Cheng, N. Liu, W.F. Wu, Studies on thermal properties and thermal control effectiveness of a new shape-stabilized phase change material with high thermal conductivity, Appl. Therm. Eng. 36 (1) (2012) 345–352, https://doi.org/10.1016/j.applthermaleng.2011.10.046.
[31] S. Mahmoud, A. Tang, C. Toh, R. AL-Dadah, S.L. Soo, Experimental investigation of inserts configurations and PCM type on the thermal performance of PCM based heat sinks, Appl Energy 112 (2013) 1349–1356, https://doi.org/10.1016/j.apenergy.2013.04.059.
[32] X.H. Yang, S.C. Tan, Y.J. Ding, L. Wang, J. Liu, Y.X. Zhou, Experimental and numerical investigation of low melting point metal based PCM heat sink with internal fins, Int. Commun. Heat Mass Transfer 87 (2017) 118–124, https://doi.org/10.1016/j.icheatmasstransfer.2017.07.001.
[33] B. Praveen, S. Suresh, Thermal performance of micro-encapsulated PCM with LMA thermal percolation in TES based heat sink application, Energy Convers. Manag. 185 (2019) 75–86, https://doi.org/10.1016/j.enconman.2019.01.080.
[34] A.N. Desai, A. Gunjal, V.K. Singh, Numerical investigations of fin efficacy for phase change material (PCM) based thermal control module, Int. J. Heat Mass Transf. 147 (2020), 118855, https://doi.org/10.1016/j.ijheatmasstransfer.2019.118855.
[35] C.R. Raj, S. Suresh, R.R. Bhavsar, V.K. Singh, K.A. Govind, Influence of fin configurations in the heat transfer effectiveness of solid solid PCM based thermal control module for satellite avionics: numerical simulations, J Energy Storage 29 (2020), https://doi.org/10.1016/j.est.2020.101332.
[36] J.Y. Ho, Y.S. See, K.C. Leong, T.N. Wong, An experimental investigation of a PCM-based heat sink enhanced with a topology-optimized tree-like structure, Energy Convers. Manag. 245 (2021), https://doi.org/10.1016/j.enconman.2021.114608.
[37] K. Kansara, V.K. Singh, R. Patel, R.R. Bhavsar, A.P. Vora, Numerical investigations of phase change material (PCM) based thermal control module (TCM) under the influence of low gravity environment, Int. J. Heat Mass Transf. 167 (2021), https://doi.org/10.1016/j.ijheatmasstransfer.2020.120811.
[38] R. Pakrouh, M.J. Hosseini, A.A. Ranjbar, R. Bahrampoury, A numerical method for PCM-based pin fin heat sinks optimization, Energy Convers. Manag. 103 (2015) 542–552, https://doi.org/10.1016/j.enconman.2015.07.003.
[39] R. Baby, C. Balaji, Experimental investigations on thermal performance enhancement and effect of orientation on porous matrix filled PCM based heat sink, Int. Commun. Heat Mass Transfer 46 (2013) 27–30, https://doi.org/10.1016/j.icheatmasstransfer.2013.05.018.
[40] S. Gharbi, S. Harmand, S. ben Jabrallah, Experimental comparison between different configurations of PCM based heat sinks for cooling electronic components, Appl Therm Eng 87 (2015) 454–462, https://doi.org/10.1016/j.applthermaleng.2015.05.024.
[41] C. Xu, S. Xu, R.D. Eticha, Experimental investigation of thermal performance for pulsating flow in a microchannel heat sink filled with PCM (paraffin/CNT composite), Energy Convers. Manag. 236 (2021), https://doi.org/10.1016/j.enconman.2021.114071.
[42] S.K. Saha, K. Srinivasan, P. Dutta, Studies on optimum distribution of fins in heat sinks filled with phase change materials, J. Heat Transf. 130 (3) (2008), https://doi.org/10.1115/1.2804948.
[43] G. Ye, G. Zhang, L. Jiang, X. Yang, Temperature control of battery modules through composite phase change materials with dual operating temperature regions, Chem. Eng. J. 449 (2022), https://doi.org/10.1016/j.cej.2022.137733.
[44] O. Younis, A. Abderrahmane, M. Hatami, A. Mourad, G. Kamel, Thermal energy storage using nano phase change materials in corrugated plates heat exchangers with different geometries, J. Energy Storage 55 (2022), 105785, https://doi.org/10.1016/j.est.2022.105785.
[45] S. Li, et al., Flexible phase change materials obtained from a simple solvent-evaporation method for battery thermal management, J. Energy Storage 44 (2021), https://doi.org/10.1016/j.est.2021.103447.
[46] C. Hu, H. Li, Y. Wang, X. Hu, D. Tang, Experimental and numerical investigations of lithium-ion battery thermal management using flat heat pipe and phase change material, J. Energy Storage 55 (2022), 105743, https://doi.org/10.1016/j.est.2022.105743.
[47] W. Wu, G. Ye, G. Zhang, X. Yang, Composite phase change material with room-temperature-flexibility for battery thermal management, Chem. Eng. J. 428 (2022), https://doi.org/10.1016/j.cej.2021.131116.
[48] RUBITHERM (GmbH), 2021.
[49] A. Abhat, Low temperature latent heat thermal energy storage: Heat storage materials, 2022.
[50] X.H. Yang, S.C. Tan, J. Liu, Numerical investigation of the phase change process of low melting point metal, Int. J. Heat Mass Transf. 100 (2016) 899–907, https://doi.org/10.1016/j.ijheatmasstransfer.2016.04.109.
[51] X.H. Yang, S.C. Tan, Y.J. Ding, L. Wang, J. Liu, Y.X. Zhou, Experimental and numerical investigation of low melting point metal based PCM heat sink with

internal fins, Int. Commun. Heat Mass Transfer 87 (2017) 118–124, https://doi.org/10.1016/j.icheatmasstransfer.2017.07.001.
[52] D. Pal, Y.K. Joshi, Thermal management of an avionics module using solid-liquid phase-change materials, J. Thermophys. Heat Transfer 12 (2) (1998) 256–262, https://doi.org/10.2514/2.6329.
[53] V.R. Voller, C. Prakash, A Fixed Grid Numerical Modelling Methodology for Convection-diffusion Mushy Region Phase-change Problems, 1987.
[54] A.D. Brent, V.R. Voller, K.J. Reid, Enthalpy-porosity technique for modeling convection-diffusion phase change: application to the melting of a pure metal, Numer. Heat Transfer 13 (3) (1988) 297–318, https://doi.org/10.1080/10407788808913615.
[55] M. Bulut, A. Kahriman, N. Sozbir, T.A.S. Rd, Design and Analysis for Thermal Control System of Nanosatellite, 2010, https://doi.org/10.1115/IMECE2010-39716.
[56] R. Karam, Satellite Thermal Control for Systems Engineers, American Institute of Aeronautics and Astronautics, 1998, https://doi.org/10.2514/4.866524.
[57] K. Yamada, H. Nagano, Development of a heat storage panel for micro/nano-satellites and demonstration in orbit, Appl. Therm. Eng. 91 (2015) 894–900, https://doi.org/10.1016/j.applthermaleng.2015.08.073.